Materials & Design 233 (2023) 112246

Contents lists available at ScienceDirect

Materials & Design

journal homepage: www.elsevier.com/locate/matdes

Development of 3D printed heavyweight concrete (3DPHWC) containing magnetite aggregate

Karol Federowicz [a], Mateusz Techman [a], Szymon Skibicki [a], Mehdi Chougan [b], Ahmed M. El-Khayatt [c,d], H.A. Saudi [e], Jarosław Błyszko [a], Mohamed Abd Elrahman [f], Sang-Yeop Chung [g,*], Pawel Sikora [a,*]

[a] Faculty of Civil and Environmental Engineering, West Pomeranian University of Technology in Szczecin, Poland
[b] Department of Civil and Environmental Engineering, Brunel University London, Uxbridge UB8 3PH, UK
[c] Department of Physics, College of Science, Imam Mohammad Ibn Saud Islamic University, (IMSIU), Riyadh, Saudi Arabia
[d] Reactor Physics Department, Nuclear Research Centre, Atomic Energy Authority, 13759 Cairo, Egypt
[e] Department of Physics, Faculty of Science, Al-Azhar University, Women Branch, Nasr City, Cairo, Egypt
[f] Structural Engineering Department, Mansoura University, Mansoura City 35516, Egypt
[g] Department of Civil and Environmental Engineering, Yonsei University, Seoul 03722, Republic of Korea

ARTICLE INFO

Keywords:
Additive manufacturing
3D printing
Heavyweight concrete
Radiation shielding
Gamma-ray
Magnetite

ABSTRACT

The main objective of this study is to develop 3D printed heavyweight concrete (3DPHWC) to produce elements with a dry density of up to 3500 kg/m^3 by replacing natural aggregate (SA) with magnetite aggregate (MA) up to 100%. A comprehensive systematic study was conducted to thoroughly assess mixtures' mechanical properties, physical proficiency, fresh properties, and printing qualities. The inclusion of MA exhibited the desired fresh properties required for 3D printing and promising physical and mechanical properties. Evaluation of the mechanical properties of designed 3DPHWC indicates that replacing SA with MA increases both cast and printed samples' strengths. The 3D printed M100 sample achieved higher 28 days flexural and compressive strengths by 18 % and 20 %, respectively, compared to printed control mix (M0). Micro-CT study correspondingly demonstrated improvements in the composites' porosity, pore size, and pore morphologies. The linear attenuation coefficients (LACs) and half-value layer (HVLs) for slow neutron and gamma-ray were measured to assess radiation shielding characteristics. A significant performance improvement was obtained for slow neutrons by introducing the magnetite aggregate. Unlike slow neutrons, no significant difference was observed between cast and printed samples against γ-rays. Moreover, the effect of porosity on the shielding performance was discussed.

1. Introduction

Nowadays, due to the complexity of the structures that accommodate radiation-generating devices, such as nuclear power plants and medical facilities, health and safety requirements should consider both the structures' mechanical performance and their ability to absorb radiation energy [1]. Radiation shielding is becoming of consideration due to increased radionuclide releases from numerous sources and environmental protection issues [2]. As a result, it is necessary to establish a protective insulation region against the radioactive radiation by positioning a protective component/barrier between the radiation-emitting source and the medium subjected to the radiation [1]. In order to develop efficient radiation absorption, numerous investigations have been carried out in which the experiments explored a range of materials, including polymers [3], glass components [4], bricks [5], rocks [6], and concrete [7]. However, concrete mixtures are identified as the most promising shielding substance owing to their superior structural and high resilience capabilities. Heavyweight concrete (HWC), a relatively cheap and available material, has been extensively used as insulation against radioactive radiation in constructions due to its high density, i.e., more than 2600 kg/m^3 [8]. Most HWCs are created utilizing heavyweight aggregates with densities greater than 3000 kg/m^3 [9–11]. Most of the total weight of HWC is comprised of aggregates, which account for 70–80% of the overall weight of the concrete, affecting the

* Corresponding authors at: Faculty of Civil and Environmental Engineering, West Pomeranian University of Technology in Szczecin, Szczecin, Poland (P. Sikora), Department of Civil and Environmental Engineering, Yonsei University, Seoul 03722, Republic of Korea (S.-Y. Chung).
E-mail addresses: sychung@yonsei.ac.kr (S.-Y. Chung), pawel.sikora@zut.edu.pl (P. Sikora).

https://doi.org/10.1016/j.matdes.2023.112246
Received 7 February 2023; Received in revised form 27 June 2023; Accepted 13 August 2023
Available online 15 August 2023

physical and mechanical properties and, consequently, the shielding performance of the structure [12]. This indicates that the quantity and nature of aggregates possess a considerable impact on the characteristics of concrete [13]. As reported by various studies, the inclusion of several types of heavy-weight aggregates, including magnetite [14], barite [15], hematite [16], ilmenite [17], and steel furnace slag [18] can induce radiation shielding properties. Magnetite has drawn more attention than other heavyweight aggregates due to its high stability, and abundance in nature [19]. For instance, Gunoglu et al. [20] examined the linear attenuation coefficients (LACs) of concretes comprising 0–75 wt% basalt-magnetite aggregates for various gamma energies. Their findings indicate that linear attenuation coefficients rise with increasing concrete density and diminish with increasing gamma energy. A study conducted by Wang et al. [19] showed that the inclusion of magnetite aggregates not only improves the mechanical and shielding performance of concrete but also enhances its electromagnetic properties and microwave deicing efficiency. As previously discussed, nuclear structures have been developed using heavyweight concrete. The nuclear reactor's neutron flux and gamma radiation increase the temperature of the reactor cover. Even though nuclear reactors typically operate at temperatures below 100 °C, they can reach 350 °C in the case of an emergency situations [21]. Therefore, HWC performance should be steady in exposure to elevated temperatures. Fire resistance has also been positively affected by magnetite aggregate inclusion. According to Ali et al. [21], the compressive strength of concrete containing magnetite remains unchanged up to 800 °C.

In recent years, concrete 3D printing has been introduced as a promising technology for intelligent construction, providing several benefits of free-formwork, flexible design, high safety, low labour demand, and material saving [22,23]. The technique has been successfully employed to build emergency infrastructures and residences with complex structures [24–26]. A digitally programmed printing path is used to extrude concrete from a nozzle and automatically place it in layers. The material needs to be flowable enough to be pumped through a nozzle and acquire sufficient stiffness and strength to maintain its geometry following layer-by-layer deposition [23,27]. Therefore, 3D printing of HWC with relatively high fresh density is challenging as the increased weight of layers results in a lower shape stability [28].

The present study deals with a novel idea of using magnetite-based heavyweight concrete as a viable feedstock for the 3D printing process. To the best of the authors knowledge no study has investigated the 3D printing of heavyweight concrete mixtures, and based on this, it is proposed to conduct a comprehensive experimental campaign to systematically evaluate the feasibility of magnetite-based heavyweight concrete mixtures for 3D printing. In this study, natural river sand aggregates were replaced by varying degrees of 20 vol%, 40 vol%, 60 vol %, 80 vol%, and 100 vol% with magnetite aggregates. A series of experiments was conducted to determine the fresh and hardened properties. All mixes were first subjected to several of experiments, including calorimetry, flow table, penetration, and uniaxial unconfined compression tests. For all cast and printed compositions in the hardened state, the impact of heavyweight aggregates on density, mechanical performance, thermal conductivity, and water absorption was subsequently assessed. Following the 3D printing of the hollow wall segments, several other parameters, such as shape stability employing the image-based correlation test, porosity using a micro-CT scan, and radiation shielding, were examined.

2. Materials and printing process

2.1. Materials

The binder materials used in this study were: i) ordinary Portland cement CEM I 52.5R obtained from Górażdże Cement (Chorula, Poland), ii) silica fume (SF) purchased from the Mikrosilika Trade Company (Poland), iii) fly ash (FA) obtained from the Dolna Odra power plant (Poland). The binder's chemical compositions and specific gravities are presented in Table 1. Natural river sand (SA) obtained locally (Bielinek, Poland) and magnetite aggregate (MA) supplied from LKAB company (Sweden) were used as an aggregate. Both aggregates were sieved to achieve a $\leq$2 mm nominal size gradation. The helium pycnometer was used to determine the specific gravities of SA and MA, which were found to be 2.63 g/cm^3 and 5.08 g/cm^3, respectively. Particle size distributions of fine aggregates and binder constituents are presented in Fig. 1 and Fig. 2, respectively. To ensure the adequate workability of the mixture a high-performance powder polycarboxylate superplasticizer Sika ViscoCrete 111 (SP) was used.

2.2. Mixture composition

As presented in Table 2, a total of six cementitious composites were produced. The reference mixture (M0) was selected based on the author's previous studies [29,30]. In this study, the natural sand aggregate was replaced by 20 vol%, 40 vol%, 60 vol%, 80 vol% and 100 vol% of magnetite aggregate (MA). For 80 vol% and 100 vol% replacement rates, the SP dosage was slightly increased to maintain its printability accordingly. The water-to-binder ratio was fixed at w/b = 0.24 for all mixes.

2.3. Mixing and 3D printing

The mixtures were prepared in the standard 110 L concrete mixer with a mixing speed of 54 rpm. The cementitious composites were prepared in two stages. In the first stage all the dry components (including SP) were mixed for about 120 s to ensure their homogeneity. Thereupon, the mixing water was gradually added to the dry-mix and mixed for another 540 s. The prepared mix was then transported manually to the pump.

The printing setup (Fig. 3) consists of a computer-controlled gantry printer (3 degrees of freedom) equipped with a connected PFT Swing M pump. The printing area is 145 cm × 145 cm × 80 cm. The pump is coupled through a 6 m long Ø1 inch hose ended with a 40 × 10 mm nozzle directed at a 45° angle or Φ15 mm round nozzle (see stability test in Section 3.3). In this study, a printing rate of 4500 mm/min was used. The extrusion rate was equal to 1.2 L/min ± 0.2 L/min for Φ15 mm round nozzle and 1.8 L/min ± 0.2 L/min for 40 × 10 mm nozzle and was adjusted during the test to achieve printed path without defects.

3. Methods

3.1. Calorimetry

An adiabatic calorimeter (Controls S.p.A., Italy) was used to measure the heat released by concrete throughout the seven-day hardening process on a 150 mm cubic specimen following EN 12390-15 [31]. Two mixes, M0 and M100, were selected for this experiment. Materials before the test were stored at an ambient temperature of 20 °C ± 2 °C.

Eq. (1) was used to measure the cumulative development of heat of hydration based on the test results.

$$q(t) = \frac{C_{con} \bullet \Delta T_c^*(t)}{m_{con}} \quad (1)$$

where: $q(t)$ is heat release at a time, C_{con} is the total heat capacity of the concrete specimen alone, $\Delta T_c^*(t)$ is intrinsic temperature rise, m_{con} is the mass of a concrete sample.

The total heat capacity of the mix was determined using the specific heat capacity of mix constituents in accordance with the EN 12390-14 [32] and literature [33]. The assumed values are presented in Table 3.

Table 1
The chemical composition, and specific gravity of binder constituents.

Component [wt%]	CaO	SiO_2	Al_2O_3	Fe_2O_3	K_2O	Na_2O	Cl^-	Other	Specific gravity [g/cm^3]
CEM I 52.5R	63.93	20	4.89	2.34	0.77	0.14	0.07	7.86	3.14
Fly ash	4.44	52.2	24.9	5.76	2.63	1.35	0.003	8.72	2.08
Silica fume	< d.L.*	91.1	0.26	< d.L.*	1.58		< d.L.*	7.06	2.20

* Below detection level.

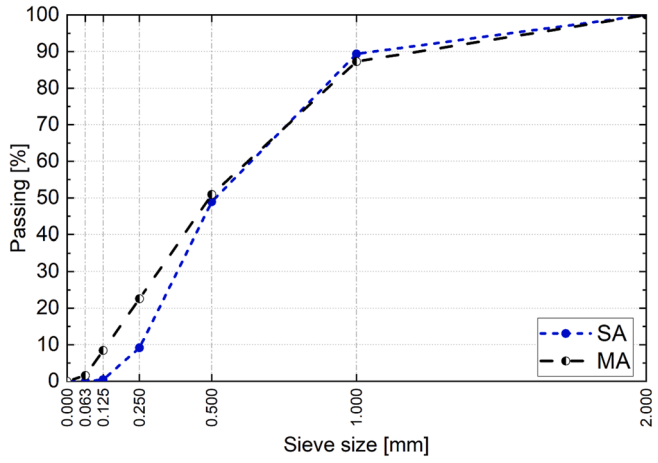

Fig. 1. Sieve analysis of river sand (SA) and magnetite sand (MA).

3.2. Fresh properties

The fresh density of mixes was determined using a standardized 1 L cylinder. The mix was compacted in two layers and weighted using an accurate scale. The measurements were performed three times and the mean value was taken as a representative.

The flow table measurements were performed in accordance with the EN 1015-3 [34]. The test was conducted at 15 min intervals up to 60 min, starting from the moment of adding the water to the mix.

The shear stress on the cementitious mixtures was evaluated by employing a manual shear vane equipment [35]. The equipment is typically used to determine the soil properties but can be adapted to evaluate cementitious mixes [36]. The measurements were performed at 15 min intervals starting from water incorporation up to 60 min.

The uniaxial unconfined compression test (UUCT), often referred to as a squeezing test, is used for the determination of the green strength of the mix. The test was performed using testing protocols employed in prior studies [37,38], in which cylindrical samples (Φ60 mm, h = 35 mm) were subjected to compression with a constant displacement rate of 30 mm/min.

Finally, the buildability performance of the mixes with the lowest (M0) and highest (M100) densities was examined using a penetration test. In this test, each mixture's static yield stress was determined to assess the material's buildability. The measurement was performed following the methodology reported by Mazhoud et al. [39]. A Vicat

Table 2
Composition of 3D printed mixes [kg/m^3].

Material	CEM I 52.5R	FA	SF	SA	MA	SP	Water
M0	580	166	83	1300	–	2.0	200
M20	580	166	83	1040	502.2	2.0	200
M40	580	166	83	780	1004.4	2.0	200
M60	580	166	83	520	1506.6	2.0	200
M80	580	166	83	260	2008.8	2.1	200
M100	580	166	83	–	2511.0	2.2	200

Fig. 3. Printing setup: gantry printer (left) and 3-layered specimen printing (right).

Table 3
Heat capacity of specific mix constituents.

Heat capacity C	OPC	FA	SF	SA	MA	Water
[J/kg*K]	840	730	730	840	779	3760

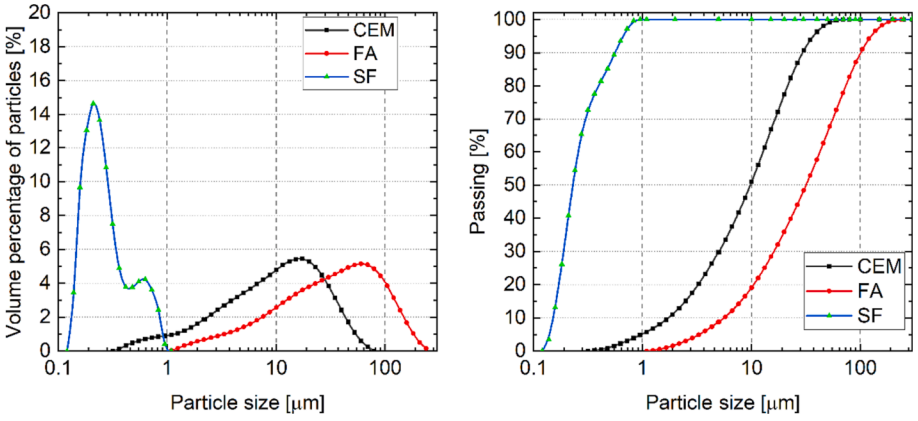

Fig. 2. Particle size distribution of binder components: percentage of particular grain size (left) and grading (right).

apparatus was used in order to determine the penetration depth (h) of the cone plunger (mass of 80 g, tip angle of 30°). The measurement started at 15 min from adding the water up to 60 min with time intervals of 15 min. Prior to the measurement mixture was extruded through the pump and vibrated to distribute the mixture in the measuring ring. Afterward, the cone plunger was released to freely penetrate the material under its own weight and the depth of penetration was recorded. Between measurements, the specimen was left exposed to simulate the yield stress development in the printing conditions (after deposition). The static yield stress of material was calculated using the following Eq. (2):

$$\tau_0 = \frac{m \times g \times \cos^2\theta}{\pi h^2 \times \tan\theta} \tag{2}$$

Where: m is the mass of the cone plunger, g is the gravity acceleration, h is the penetration depth, and θ is the tip angle of the cone plunger.

The experimental results were compared with the theoretical calculations following Eq. (3) presented by Perrot et al. [40] using Eq. (3).

$$\tau_0 = \frac{\rho g H}{\sqrt{3}} \tag{3}$$

Where ρ, g and H are the density of the fresh mixture, gravitational force and final height of the printed object, respectively.According to [40], to prevent the collapse of a printed specimen, the yield stress of the bottom layers must always be higher than the stress generated by the weight of the top layers.

3.3. Shape stability evaluations by image-based measurements

Each mixture was printed to produce a rectangular hollow wall segment of 400 mm × 300 mm with rounded corners (see Fig. 4). All the wall elements were printed in 42 layers (i.e., 503 mm ± 2 mm). The wall elements were printed using a Φ15 mm round nozzle with a horizontal trowel at a constant printing speed of 4500 mm/min, the extrusion rate was equal to 1.2 L/min ± 0.2 L/min and was adjusted during the test to achieve printed path without defects. The printing of wall elements started approximately 20 min from mixing the material with a total printing time of ~12 min (ca. 17 s per layer). Fig. 5 presents the example of wall segments directly after printing walls.

The layers' deformation (change in height) was assessed during printing using image analysis. Reference points were manually inserted in the bottom layers to enable deformation measurements. The images were then processed using a specially coded algorithm in the OpenCv2 version for Python (Python - version 3.9, OpenCv-python 4.6.0.66). The analyses were carried out to assess the influence of heavyweight aggregates on the shape retention of the bottom layers. The information about the deformation of bottom layers could help to establish setup printing parameters, including the velocity of the nozzle and pump output.

Each wall element was filmed using a Nikon D5100 camera at 24 fps during the printing process. The video was then split into high-resolution frames, and every frame was divided into smaller pictures to improve the line detection system. Fig. 5 shows the algorithm's operation, in which the 3-channel (RGB) photo was converted into a single-channel (GRAY) image. For this purpose, RGB2GRAY functions were used. The second stage of the algorithm is presented in Fig. 6. Based on the analysis of gray scale values, the interlayer zones were detected. Fig. 6a) shows various vertical lines of interest for measuring the deformation. Fig. 6b) presents the example of chosen section used for the detection. In Fig. 6c), the blue line represents the gray scale values, while the local minima of the function that show the interlayer zone locations are marked as red dots. The written algorithms, using the initially input value of layer height select the appropriate section for seeking the minima values. The final analysis considers a minimum of ten lines to appropriately evaluate the layer height. It should be mentioned that the measurements can be made for a higher number of layers, however it increases the measurement error due to possible surface defects.

3.4. Hardened properties

Two types of samples (cast and printed) were prepared to determine

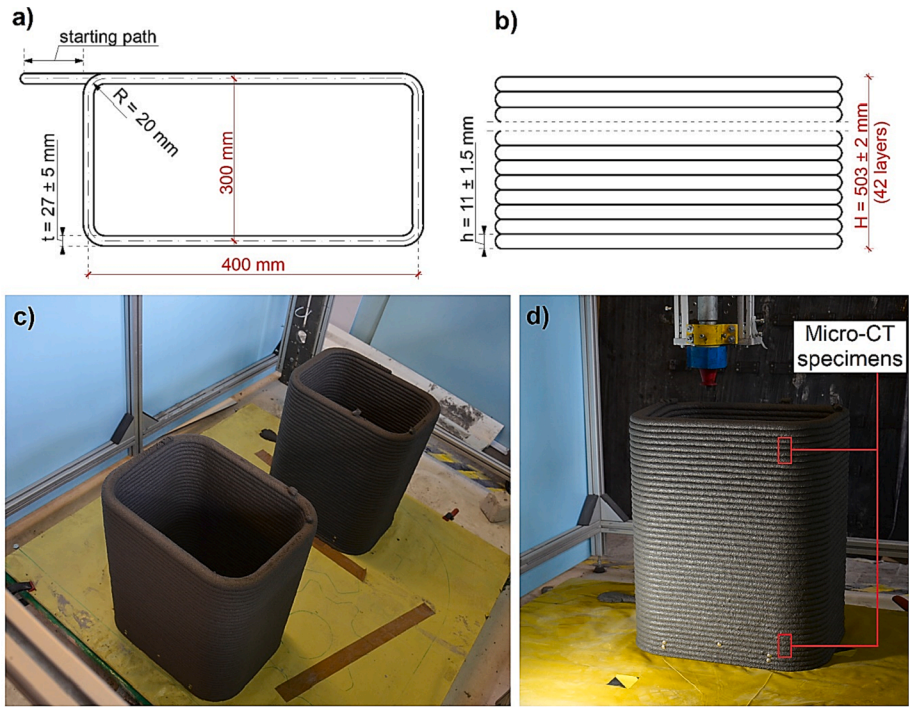

Fig. 4. Plan of the printed wall (a), front view of the printed wall (b) and wall segments after printing: M20 and M40 mixes (c), M100 mix with an extraction area of specimens for micro-CT evaluations (d).

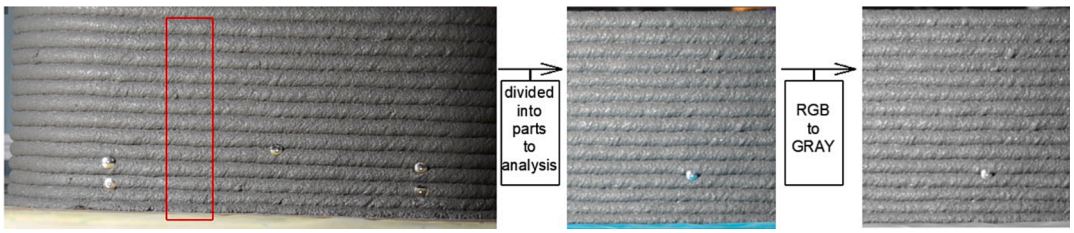

Fig. 5. Diagram of the algorithm for interlayer line detection – part 1.

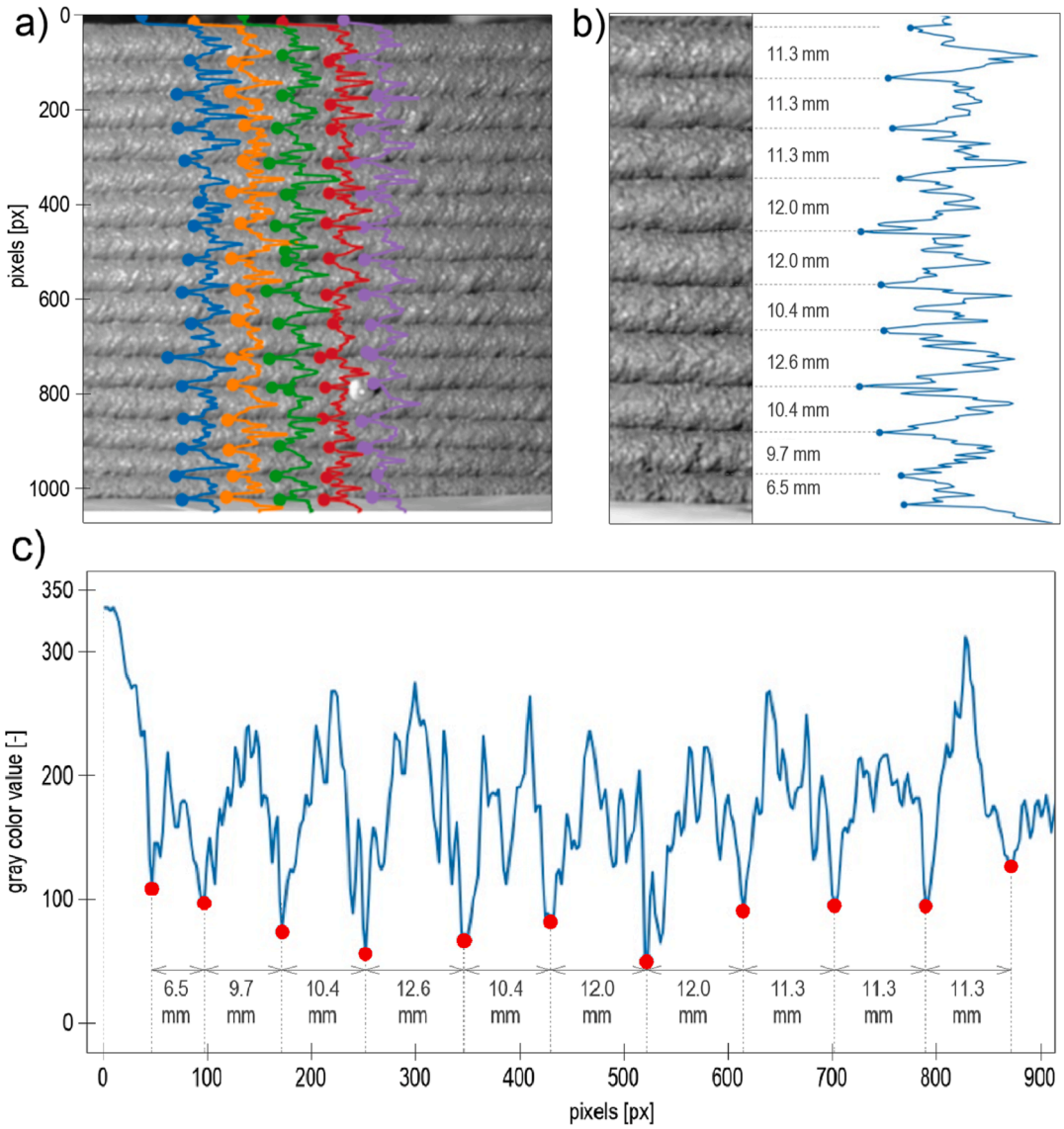

Fig. 6. Diagram of the algorithm for interlayer line detection – part 2: a) Example of lines of interest for height detection; b) Example of chosen layer height detection; c) measured layer height.

the hardened properties. First, all the mixtures were cast following EN 1015-11 [41] with dimensions of 40 mm × 40 mm × 160 mm. Then, mixtures were printed in a straight line of four layers using a 40 mm × 10 mm nozzle. After initial hardening, the samples were saw-cut to 40 mm × 40 mm × 160 mm dimensions. The specimens were stored under foil for 24 h. Thereupon, the samples were stored in the ambient conditions (i.e., T = 20 °C ± 2 °C and RH ≥ 95%).

The oven-dry density was determined on both cast and printed samples after 28 d of curing. To ensure the measurement's accuracy, the volume of samples was defined on a hydrostatic scale. The specimens (n = 3) were then oven-dried at 105 °C until a constant mass was reached and the mean value was taken as a representative.

The thermal conductivity of the mixes was evaluated using the Hot Disk transient plane source method as per ISO 22007-2 [42]. After 28 d of curing, the prismatic specimens were oven-dried at 105 °C and cooled down to the ambient temperature at zero humidity conditions. Five measurements were performed for each mix to increase the accuracy. The mean of five results was taken as the final value of thermal

conductivity.

The capillary water porosity (open porosity) of specimens was tested using the water displacement method. After 28 d of curing the specimens were removed from a water tank (T = 20 °C ± 2 °C) and their saturated masses and saturated surface dried masses were determined using a hydrostatic scale. The specimens (n = 3) were then oven-dried until a constant mass was reached and open porosity was calculated [43] with the mean value taken as a representative.

The mechanical performance (i.e., flexural strength and compressive strength) of 3D printed mixes was evaluated after 7 and 28 days of curing. The flexural strength was determined on the previously described prism samples (n = 6), while the compressive strength was assessed on the broken halves of specimens acquired in the flexural strength test (n = 12). Both tests were performed in a vertical plane to the printing direction. The mean values were taken as a representative.

3.5. X-ray micro-computed tomography

In addition to the measured properties, microstructural characteristics, such as pore and solid structures, significantly affect the quality of the printed materials. To examine the microstructural characteristics of the printed materials with different amounts of magnetite aggregate, X-ray micro-computed tomography (micro-CT) was utilized. Micro-CT is a representative non-destructive inspection method and has been used to investigate cement-based composites including 3D printing materials [44–47]. Fig. 7 describes the micro-CT imaging process. For the measurement, an X-ray passes a target specimen, and a series of cross-sectional images can be achieved by reconstructing the scanned data. In general, the reconstructed micro-CT images are expressed in 8/16-bit grayscale, and each pixel value is determined according to the relative density of a particle.

The main objective of the use of micro-CT images was to examine the pore structures of the specimens, and for this purpose, proper segmentation was required for a more effective investigation. In Fig. 7, a proper threshold was determined using the Otsu and manual selection [48], and the reconstructed image can be binarized. In the 2D binary image, the white represents the pores within the micro-CT image. A series of reconstructed and binarized images were then stacked subsequently so as to produce a 3D image of the specimen and its pore structure. In 3D volume, the gray represents the pores within the specimen. The pore characteristics were investigated using the volumetric data of each specimen obtained from micro-CT imaging. The volumetric images used in this study are composed of 600 × 400 × 1200 pixels (voxels) for $x \times y \times z$ directions with the 34.91 μm /pixel, which is enough size to describe pores that affect the material properties.

In addition, the characterization of solid phases can be performed using micro-CT data. For instance, as shown in Fig. 8, the pores are visible as black (blue markings), while a phase with high density, magnetite, presents itself with bright gray colour (red markings). In Fig. 8, it is confirmed that there was no sign of the magnetite aggregate in the M0 specimen. From this information, the relative densities of the specimens with different amounts of magnetite aggregate can be compared, and the 3D micro-CT data was used to examine the solid characteristics of the materials.

3.6. Radiation shielding properties

The radiation testing experiments were performed, via the narrow beam geometry to evaluate the shielding ability against neutrons and γ-rays. A collimated narrow beam emitted from a ^{241}Am-Be neutron source with an activity of (3.7 GBq) and a BF_3 detector were employed (Fig. 9a). A moderated neutron beam with known intensity was used to an incident on the investigated samples. For the gamma-ray measurements, a pre-calibrated Na (Tl) detection system was used to record the incident (I_o) and transmitted (I) photons (Fig. 9b). A certain distance was kept between the source and detector to minimize the backscatter contributions. Different thicknesses were obtained by successive assembly of smoothed samples to avoid gaps that would worsen the shielding capacity. The counting time was adjusted to maintain the statistical count uncertainty at ±3%.

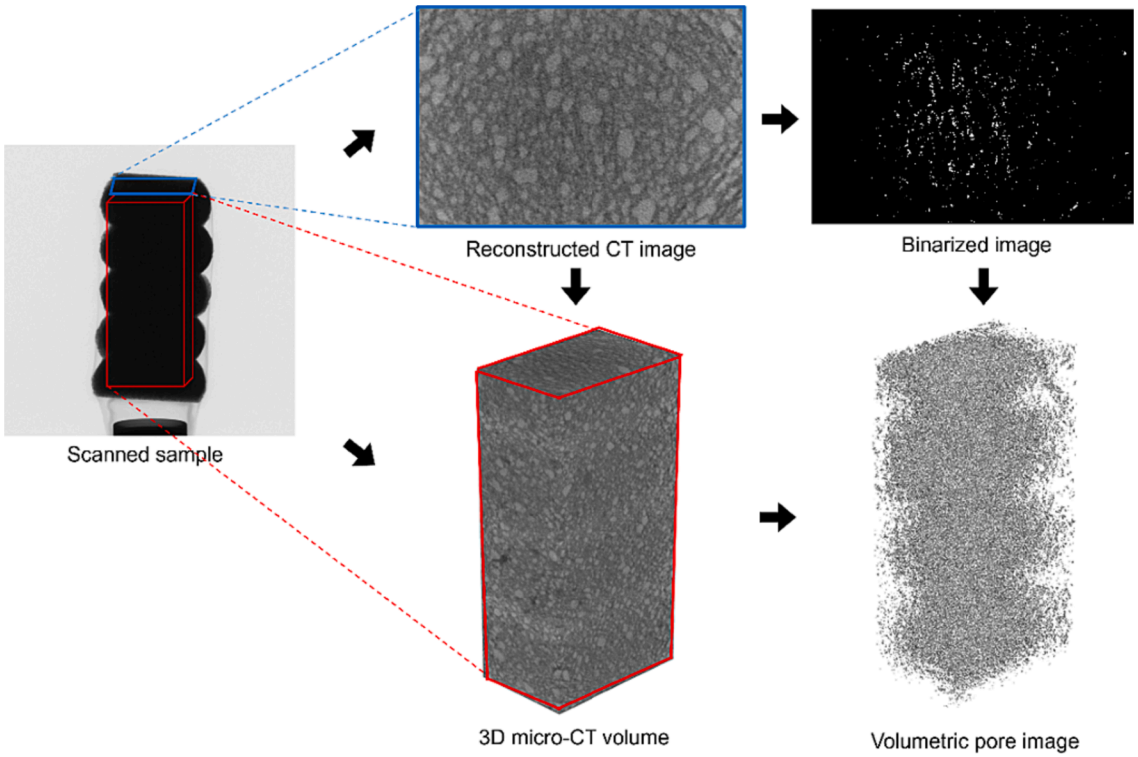

Fig. 7. Micro-CT imaging process to segment pores and solid parts (Note: in the binary images, the white represents the pores inside the specimen, while the pores are described in gray in 3D volume.)

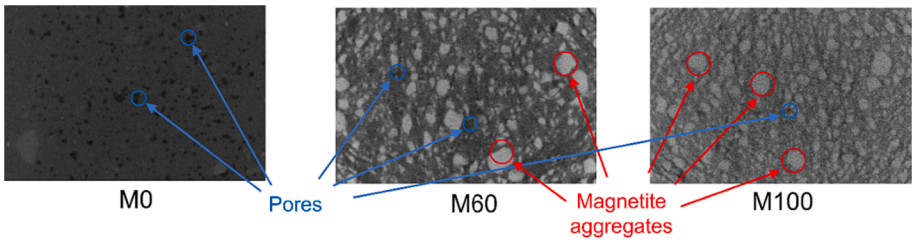

Fig. 8. Comparison of micro-CT images for each case (Note: in the images, the bright part (red) indicates magnetite aggregates, and the dark (blue) indicates pores.)

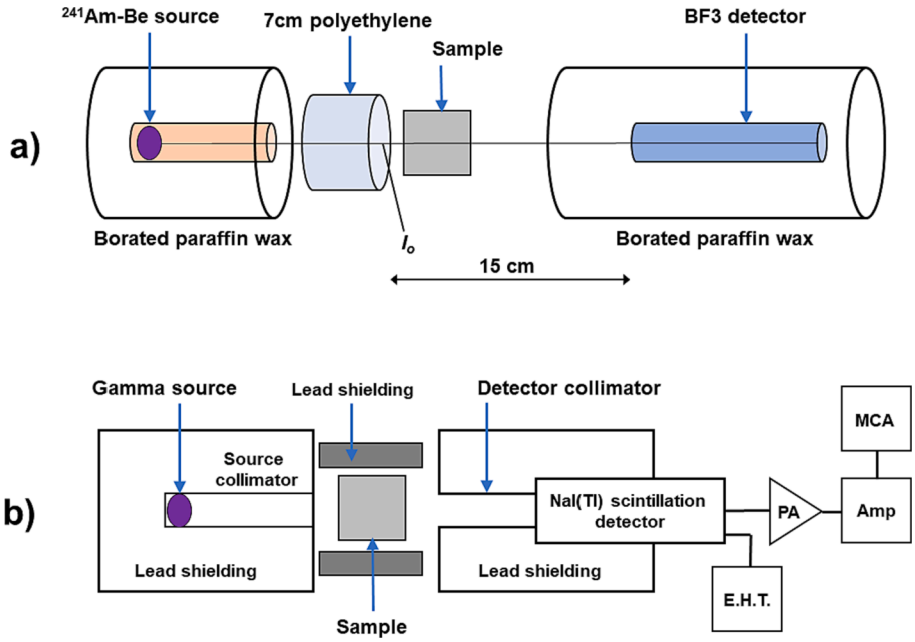

Fig. 9. The experimental setup of slow neutron transmission (a) and gamma-ray transmission (b). Reproduced from Sikora et al. [49] with permission of Elsevier (2021).

To estimate the attenuation coefficient, incident (I_0) and transmitted (I) photo-peaks were measured, and Lambert law was employed. For each concrete mix, different thicknesses were used, and the linear attenuation coefficient, LAC (μ), was calculated from the slope of the linear plot of $ln(I/I_0)$ as a function of the sample thickness (x) following Eq. (4):

$$\mu(cm^{-1}) = -\frac{1}{x}ln(I/I_0) = -\frac{1}{x}ln(T_\gamma) \quad (4)$$

Where: T_γ is the gamma-ray transmittance; $T_\gamma = (I/I_o)$.

Details of the counting system were described in our previous work of authors [49].

4. Results

4.1. Fresh properties

4.1.1. Calorimetry

For assumed and presented in Table 3 values of heat capacity the total heat capacity of a 1 m^3 of the fresh mix was determined as $C_{con,M0}$ = 2522370 J/K and $C_{con,M100}$ = 3387191 J/K. The density of the M100 mix was about 58% (Table 4) higher than the reference mix M0, while the total heat capacity was only 34% higher. Calculating the specific heat c for M0 and M100 we obtain the values of 1081.9 J/kg*K and 956.1 J/kg*K, respectively.

Conducted experiments confirm higher values of the heat capacity of the mix with magnetite aggregate. During the hydration process under adiabatic conditions, the observed increase in the temperature of the sample reached 62.61 °C and 50.03 °C for M0 and M100 respectively Fig. 10.

Table 4
Fresh density of 3DPHWC mixes.

Mixture	M0	M20	M40	M60	M80	M100
Fresh density [kg/m^3]	2240 ± 17	2480 ± 12	2746 ± 21	3011 ± 23	3282 ± 34	3541 ± 32

Using the MA as the replacement for natural sand reduces the development of the concrete's temperature, resulting in a limited risk of thermal cracking in the cooling down phase of the element. Replacement of natural sand with magnetite aggregate does not significantly affects the temperature's development curve in the initial hours of the hydration process. Both mixes reached their peak temperature after approximately 48 h. The differences in the values result not from the hydration process, as it is similar in both cases, but from the higher heat capacity of the magnetite mix.

The values of the q(t) function (Eq. (1)) calculated are 67735.6 J/kg and 47833.9 J/kg for M0 and M100, respectively.

4.1.2. Fresh density

Table 4 presents the results of the plastic density of concretes. As expected, the replacement of river sand with heavy-weight MA led to a gradual increment of concrete's fresh density by 11%, 23%, 34%, 47%,

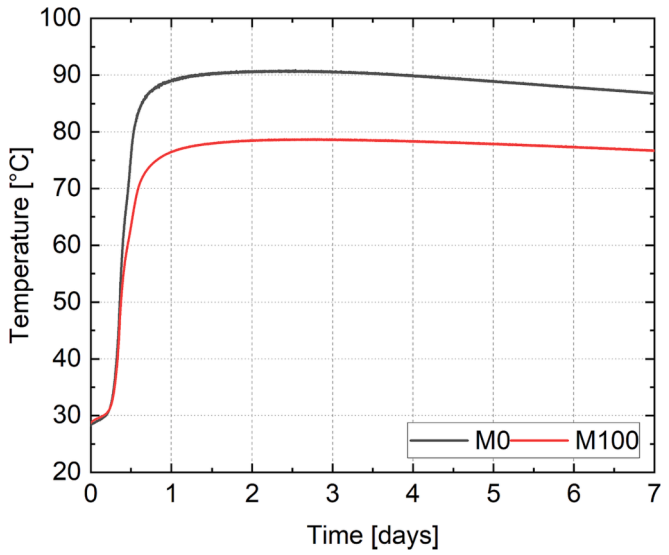

Fig. 10. Temperature development during the first 7 days for M0 and M100 mixes.

and 58% for the M20, M40, M60, M80, and M100 mixtures, respectively when compared to that of control (M0) mix (i.e., 2240 kg/m^3).

4.1.3. Flow table at time intervals

Fig. 11 presents the results of the spread diameter determined at time intervals using a flow table method. All of the mixes at the initial determination of slump flow (t = 15 min) exhibited a flow of 160 ± 10 mm. Studies have shown that mixes designed for 3D printing should exhibit slump flow in the range of 130 mm–210 mm [27]. A slightly higher spread diameter was reported for specimens M80 and M100 which could be attributed to higher SP content in the mixture. However, the trajectory of change in the slump flow at all time intervals was similar for all of the mixes used in the study and all mixtures exhibited satisfactory flow to be extruded up to 60 min.

4.1.4. Shear vane at time intervals

Fig. 12 presents the results of the shear vane test at different time intervals. A clear increment of shear stress in mixtures with increasing magnetite aggregate content was registered. The shear vane testing apparatus has been mainly used for soil testing [50]. However, it is also employed to determine the characteristics of 3D printed materials [51,52]. The recommended shear stress value to pass printability obtained in the shear vane apparatus is between 0.3 kPa and 0.9 kPa [53,54]. Despite that some parts of the presented results indicated smaller than 0.3 kPa shear stress values, printing tests proved that the workability properties of mixes were enough to maintain the weight of deposited layers. In addition, higher shear stress values reported for the mixes containing magnetite aggregates can be attributed to the characteristics of fine magnetite aggregates which, in contrary to natural river sand, is obtained from the rock crushing process; thus, the effect of mechanical interlocking of aggregate particles is reported.

4.1.5. Uniaxial unconfined compression test

Fig. 13 presents the results of the uniaxial unconfined compression test (UUCT) at different time intervals. UUCT shape of stress–strain curves changes with time increase. Therefore, for each interval, specific deformation levels were chosen for further analysis. For the interval of t = 15 min, a fixed value of deformation stress exact to 0.3 was selected as most of the curves tend to be linear within this range. For other intervals, reference deformation was fixed at 0.2. Table 5 presents stress at a set strain level recorded during the UUCT. It was clearly observed that the highest mechanical performance was achieved for mixtures containing mixed aggregate. Regardless of the time interval, the mixes M40 and M60 exhibited the highest green strength. It is worth mentioning that the mixes with only a single type of aggregate (i.e., M0 and M100) had the lowest green strength in carried-out tests (Fig. 13). This phenomenon is contacted with optimal aggregate composition, in other words, optimal particle packing between natural river sand and crushed MA particles.

After 15 min, all of the mixes tend to have significant self-deformation. It is connected with two factors: firstly, after such a short period of time hydration process is still inactive, so the green strength of mixtures was very low. Secondly, during the sample preparation for UUCT, extensive compaction, and vibration were applied that changed the rheological properties of materials. Additionally, the available apparatus has certain inertia measurements due to the weight of the upper plate where the force sensor is mounted (initial load is equal to ~2 N, which for tested samples generates 0.6 kPa).

In the following time intervals, initial deformations significantly decreased, reaching 0 mm at 60 min. The result was caused by the

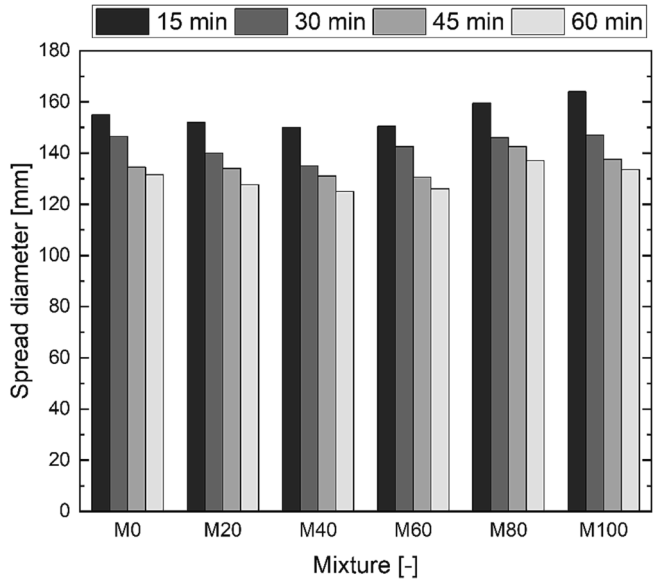

Fig. 11. Consistency of mixtures up to 60 min.

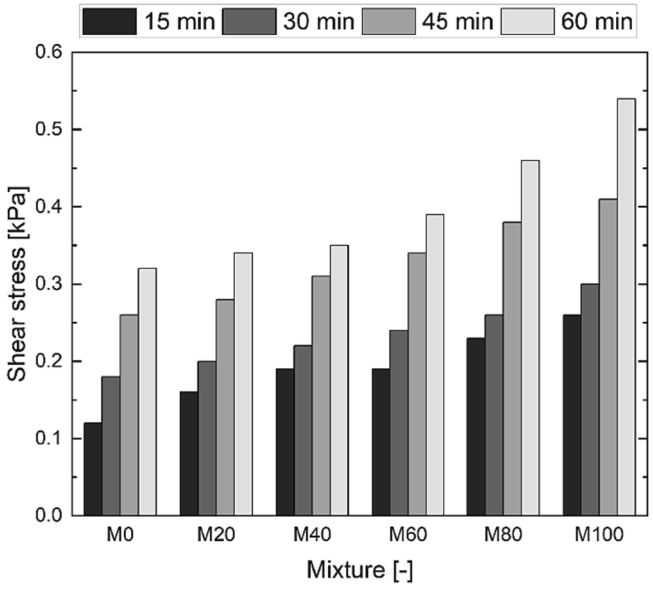

Fig. 12. Results of the shear stress determination of fresh mixes.

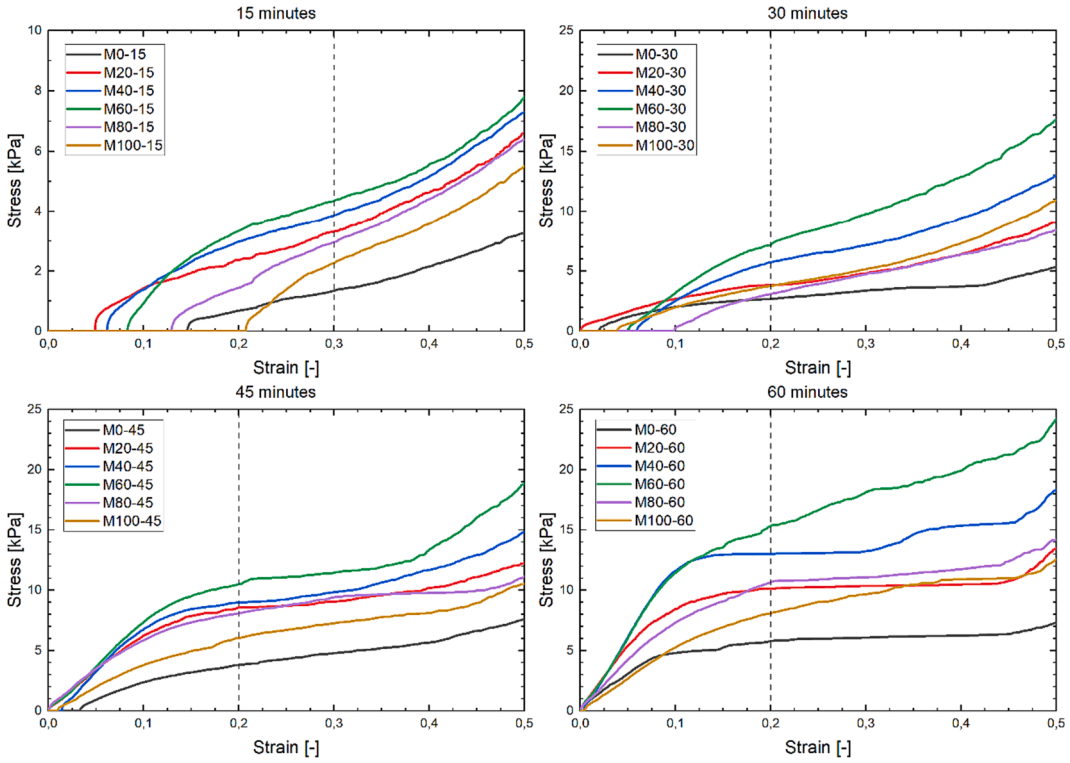

Fig. 13. Results of the uniaxial unconfined compression test at different time intervals.

Table 5
Stress at designated deformation in UUCT.

	Stress [kPa]			
	15 min	30 min	45 min	60 min
M0	1.35	2.69	3.81	5.77
M20	3.32	3.85	8.57	10.15
M40	3.87	5.74	8.98	13.03
M60	4.35	7.18	10.49	15.34
M80	2.98	3.10	8.11	10.66
M100	2.28	3.77	6.04	8.07

stiffening of the sample in time. After 30 min from mixing of the ingredients, stress–strain curves are found to be similar to the ones at 15 min with an obvious increment in green strength. There is a lack of sharp inflection points, which indicates that no shear failure occurred.

After 45 min, mixes with mixed aggregates tend to have a visible plateau region in the stress–strain curve. That indicates that even though materials were still in a plastic state, the relation between stress and deformation was linear as in an elastic state. After reaching a strain of 0.2 mixes with both SA and MA exhibited a decline in the slope of the curves, which is related to the yielding of material. That phenomenon can be clearly seen for samples tested at 60 min. In every evaluated time interval the mixed aggregates mix (M60) had the highest green strength compared to the base mix M0.

The received in UUCT values are in line with other research on this topic. For example, Wolfs et al. [51] received up to 7.71 kPa after 15 min and up to 15.52 kPa after 60 min. Ding et al. [55] received up to 17.67 kPa after 60 min. Skibicki et al. [56] received up to 9.78 kPa after 15 min and up to 15,82 kPa after 45 min. To sum up, in this paper UUCT test results ranged between 1.35 kPa and 15.34 kPa which are in agreement with other studies and prove suitability for printing.

4.1.6. Static yield stress development

Fig. 14 depicts the measured static yield stress of the mixtures containing 100% SA (M0) and 100% MA (M100) at various rest intervals of 15 min. As reported in previous studies [40,57], printable cementitious composites' buildability and shape retention are directly associated with the static yield stress of mixtures. In order to prevent the printed specimen from collapsing, the yield stress of the bottom layer has to be higher than the stress imposed by the weights of the top layers [58]. This implies that throughout the printing process, the calculated yield stress values should never be higher than their corresponding experimentally measured values.

As demonstrated in Fig. 14, throughout the printing process (i.e., between 20 min and 32 min), slightly higher values for the measured yield stress compared to calculated values were registered for both the M0 and M100 mixes. This demonstrates that the selected compositions were adequately buildable and could be applied to medium-scale printing.

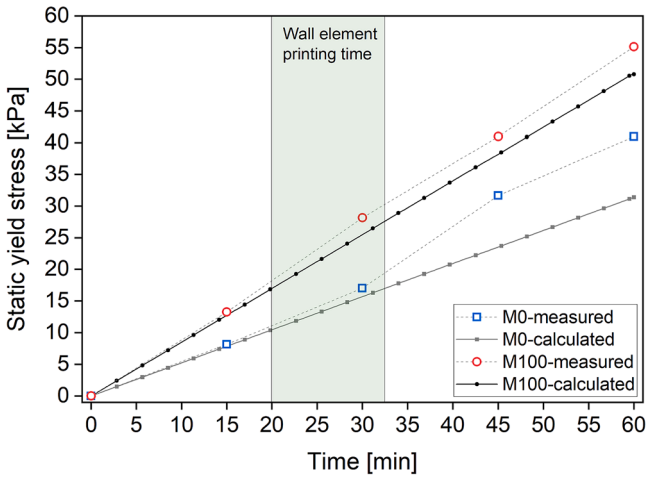

Fig. 14. Experimental and theoretical static yield stress development in studied mixes.

4.2. Shape stability evaluations by image-based measurements

Fig. 15a) and b) present the use of the algorithm described in Section 3.3 for a M0 mix. Fig. 15a) shows the measurements for the initial seven printed layers. Fig. 15b) shows the measurements after the extrusion of 42 layers (end of the printing process) for the same section. Fig. 15c) and d) show the results for corresponding sections for mix M100.

The layer thickness variations during the extrusion process are depicted in Fig. 16. Due to the printing set up and pump performance, the printed layer had a slightly larger height than theoretically assumed in the code. The subsequent layer then deforms the layer below. In the study the deformation of the 3rd layer has been taken into account. The change of the layer height caused by printing additional ~40 layers was measured. The printing process has changed the height of the 3rd layer by 1.7 mm to 2.1 mm, depending on the mix (M0: 2 mm; M20: 2.1 mm; M40: 1.7 mm; M60: 2 mm; M80: 1.7 mm; M100: 1.8 mm). However, no correlation was identified between the type of mix and the changes in layer height during this process. As seen in Fig. 16, the thickness of the 3rd layer is almost unchanged during the whole printing process. It should be noted that the deviations in the thickness (±0.3 mm) were caused by measurement errors due to a change in light exposure.

A slight variation in layer height results from printing process drawbacks depicted in Fig. 16. Even though there are up to 2.1 mm changes in layer thickness, the extrusion process leaves the layer height constant. The aforementioned issue, which is related to the measurement technique's inaccuracy and the behaviour of the printing material during extrusion by a circular shape nozzle, did not impair the shape stability of the printed structure. The presented analysis proves that the layer height did not considerably change following the extrusion procedure. The aforementioned phenomenon demonstrates that the layer's strength and stiffness were sufficient to sustain the dead load (self-weight of structure load) during printing. The proposed methodology may be used to monitor and assess the layer height to prevent structural collapse.

4.3. Hardened properties

4.3.1. Oven-dry density, thermal conductivity, open porosity

Fig. 17a presents the results of the oven-dry density of printed and cast specimens after 28 d of curing. There was no significant difference between printed and cast samples. In general, cast specimens exhibited slightly higher densities connected with better compaction due to the

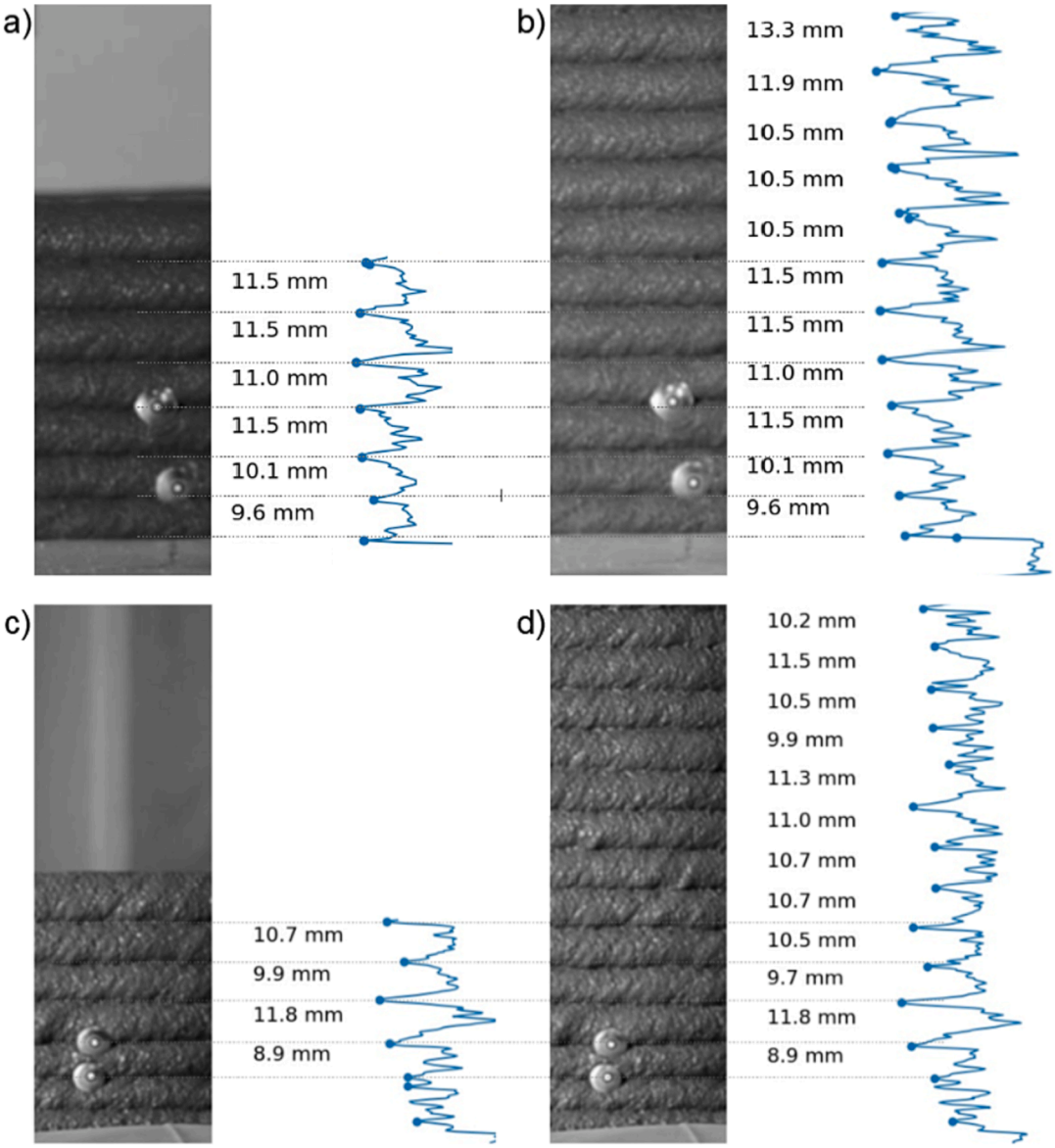

Fig. 15. Example of usage the algorithm: a) for mix M0; b) for mix M100.

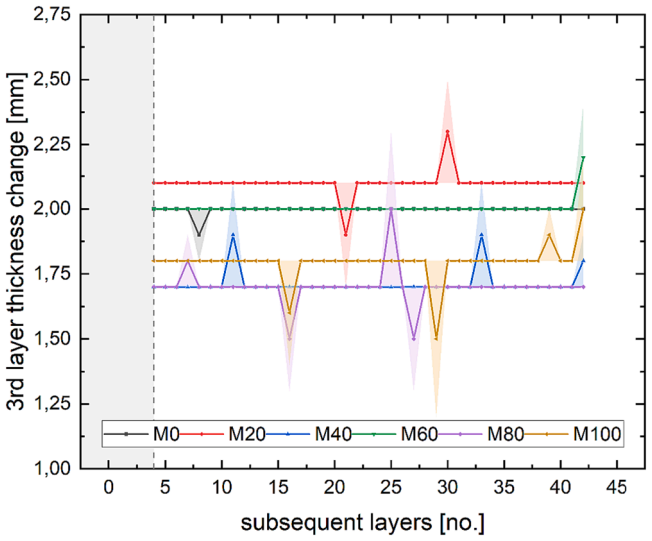

Fig. 16. Change in the height of the 3rd layer caused by the printing process with measurements errors.

vibration process during forming specimens. As expected, a gradual increment in the density of mixtures, along with an increment of the magnetite volume, was reported. To achieve a heavyweight mix conforming to the requirements of EN 206 [59], a minimal replacement ratio of 40 vol% (mixture M40) was required. Despite slight differences in the oven-dry density values, regardless of production type (printed or cast), M20, M40, M60, M80, and M100 exhibited higher oven-dry density by 10%, 22%, 33%, 44%, and 54%, respectively, when compared to corresponding control (M0) mix.

Fig. 17b presents the results of thermal conductivity and volumetric heat capacity of developed 3DHWC determined on cast specimens. Those samples were chosen as a representative due to the perfectly even surfaces required for the probe in order to determine the thermal characteristics of the material. A clear trend in the rise of thermal conductivity values along with the increment of MA content in the mixture is visible, which is related to the noticeable higher thermal conductivity of magnetite aggregate than natural sand [60]. An almost linear correlation between the oven-dry density and thermal conductivity of mixes was found (Fig. 17c). On the contrary, inclusions of magnetite aggregate did not affect the volumetric heat capacity of the concretes. These observations are in line with previous studies [33,60,61] showing that magnetite aggregate exhibits slightly lower specific heat values than natural sand, which was also reflected in the adiabatic calorimetry test results (Section 4.1).

Fig. 17d presents the results of the open porosity of print and cast specimens. The printed samples exhibit higher open water porosity than cast samples, regardless of the mix composition. This phenomenon is attributable to inter-layer connections produced as a result of layer deposition which is known to exhibit higher porosity than the bulk part of the material [62]. Therefore, besides surface absorption, the water can additionally penetrate into the interlayers connection [54]. Slightly higher open porosity values of printed specimens containing magnetite were found, which could be attributed to higher porosity of inter-layer regions which was confirmed by the micro-CT study (Section 4.4). For cast specimens up to 80 vol% SA replacement with MA there is a visible trend that with the increase of aggregate replacement ratio, the open porosity also increases. Afterward, a decrement of open porosity values is visible in M100 specimen, however, the obtained value is still higher control M0 specimen. Therefore, it can be concluded that the inclusion

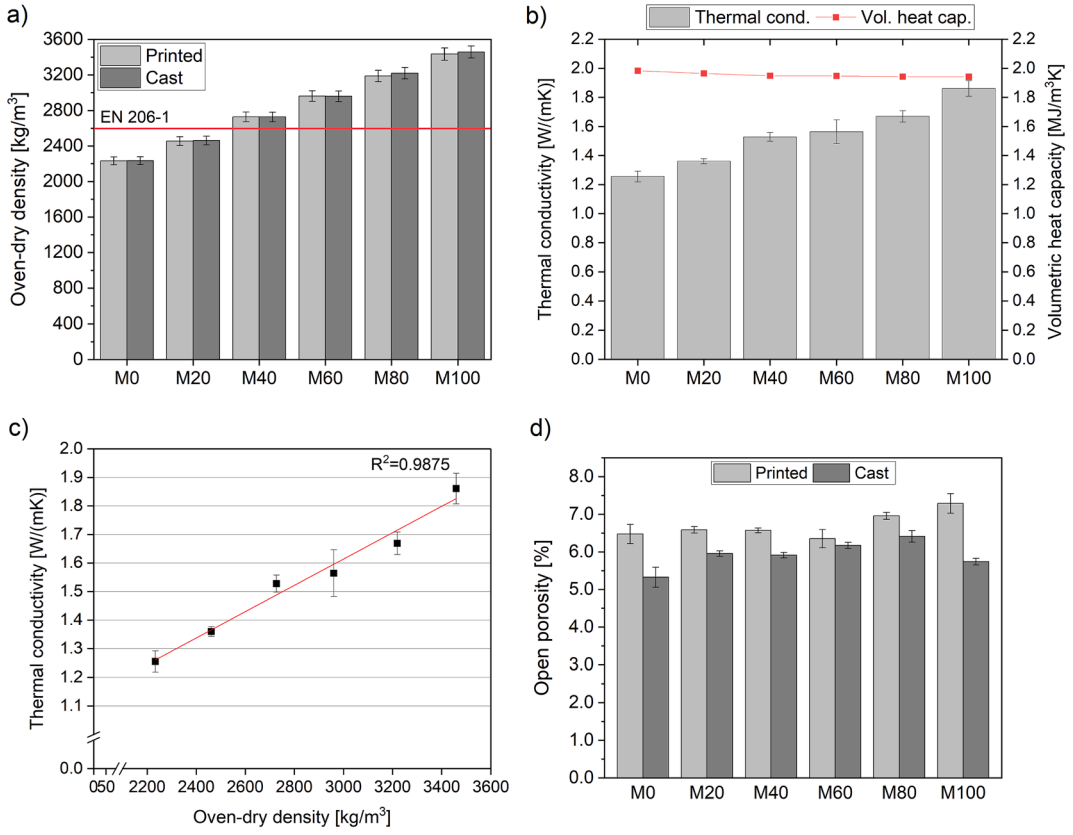

Fig. 17. Oven-dry density of concretes with the indication of the required (minimum) density of heavy-weight concrete according to EN 206 [59] (a), thermal conductivity and volumetric heat capacity of 3DHWC (b), thermal conductivity as a function of oven-dry density of cast specimens (c), open porosity of printed and casted specimens (d).

of magnetite aggregates slightly increases the open porosity of concrete, however, differences are not substantial.

4.3.2. Flexural and compressive strength

Results of the flexural and compressive strengths are presented in Fig. 18 and Fig. 19. Evaluation of the flexural strength of designed mixes indicates that replacing SA with MA gradually increases strength in both cast and printed samples. In both cast and printed samples, after 7 days of curing, the difference is clearly visible and varies from 11% for cast specimens to 18% for printed samples. There is a remarkable difference between cast and printed elements. For each mixture, the reduction of the flexural strength after 7 days due to printing process is between 30% and 36%. After 28 days trends are the same but the reduction level for flexural strength in printed samples increased to roughly 20%. It has been observed that throughout the curing time, standard deviation and coefficient of variation increase for both cast and printed specimens. One feasible reason can be the extensive autogenous shrinkage of materials despite wet curing, which generates micro-cracks in the cement matrix [63].

In terms of compressive strength in both type of samples (cast and printed) after 7 days difference caused by sand replacements is not as clearly visible as in flexural strength and vary from 7% for cast specimens to 11% for printed ones. The printing process and sample preparation affect compressive strength and decrease it by 27% to 32% after 7 days. After 28 days trends are the same, but the reduction level for compressive strength in printed samples changed to 30% up to 39% for M100 and M0, respectively. The literature survey revealed that the addition of hematite to concrete has a positive effect on its compressive strength. For example, Gencel et al. [64] found that incorporating hematite into concrete, at ratios of up to 50% of the aggregate used, can increase the compressive strength by up to 14.3% compared to plain concrete.

4.4. Microstructural characteristics from micro-CT

The micro-CT was used to investigate the inner characteristics of the materials with different dosages of magnetite aggregates. In particular, the pore characteristics, such as closed porosity, pore sizes, and shapes, were examined, and a relative solid density was also evaluated. Here, the pores larger than the used pixel size (34.91 μm) were only considered. Since the pore structure is one of the most dominant factors which affects the mechanical and thermal properties of cement-based composites including 3D printed materials, it is highly desired to characterize the pores in detail. Here, the representative cases, M0, M60, and M100 were selected. The measured specimens were selected from the top and bottom parts of the whole printed structure to figure out the consistency according to the material height (Fig. 4d).

Fig. 20 shows the pore volume of each sample at different positions. In these binarized volumes, the gray represents the pores within the specimens, while the solids are invisible. The porosity values computed based on the obtained volume data are presented in Table 6. In this measurement, the closed pores larger than 34.91 μm were only taken into account, considering the used voxel size. As can be seen in Table 6, the measured porosity tends to decrease as the amount of magnetite aggregates increases, although there is no clear trend at the top and bottom parts of each case; this indicates that the printed samples can be considered homogeneous in general, and the materials with magnetite aggregates tend to be denser structures without closed pores. In the pore images, it can be found that there are regions without pores between the layers, and this phenomenon becomes clearer in the M100 specimen. Since the magnetite aggregates have a higher density than the binder part, the regions where the magnetite aggregates are dispersed have almost no pores, and this contributes to the relatively low porosity in terms of closed pores.

For a more detailed investigation of the pore structures, the pore characterizations were performed using the obtained micro-CT data. In general, the pore distribution of the 3D printed material can be affected by the sample height considering the printing procedure. Fig. 21 and Fig. 22 show the porosity information according to the specimen height. In Fig. 21, absolute porosity according to the specimen height is presented. It seems that the fluctuation in the absolute porosity is larger in the M0 and M60 specimens for both the top and bottom parts because the difference between the maximum and minimum porosity is about 10 %, which can be considered that the materials are inhomogeneous. To confirm the heterogeneity of the porosity of the specimens, the porosity data in Fig. 21 was normalized by dividing it into the total porosity of each specimen, as presented in Fig. 22. As shown in this figure, although the fluctuation of the absolute porosity was relatively small in the M100 specimen, the difference of the normalized porosity according to the height is distinct in the M100 specimen; this indicates that the heterogeneity of the porosity is larger in the specimens with more amount of the magnetite aggregates, and it can be noticed that the inclusion of

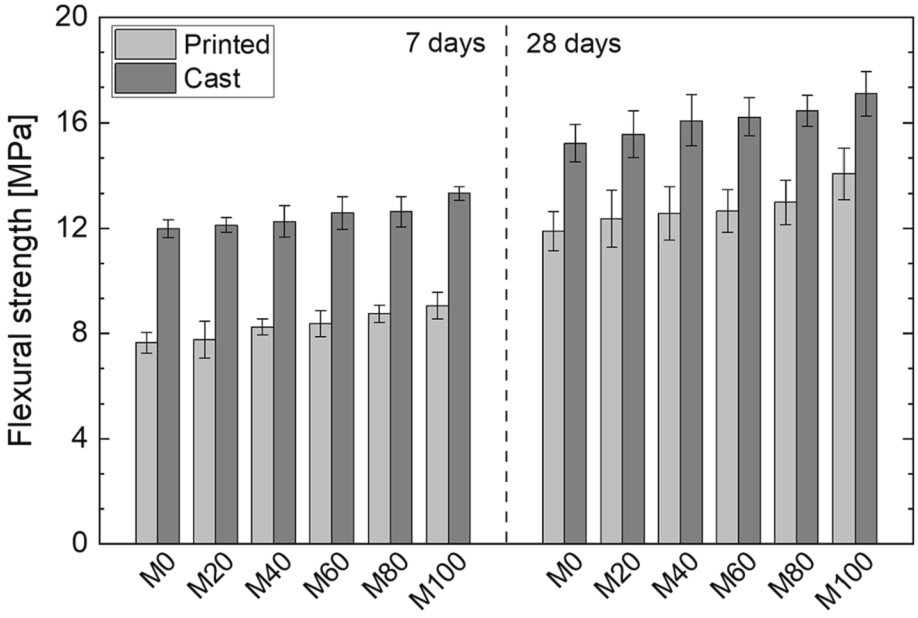

Fig. 18. Flexural strength of printed and cast specimens.

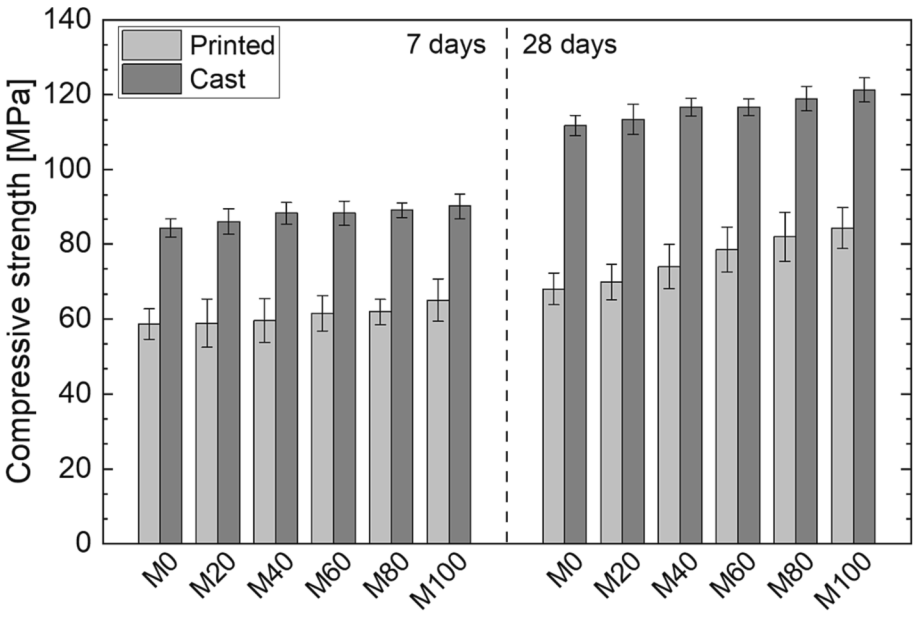

Fig. 19. Compressive strength of printed and cast specimens.

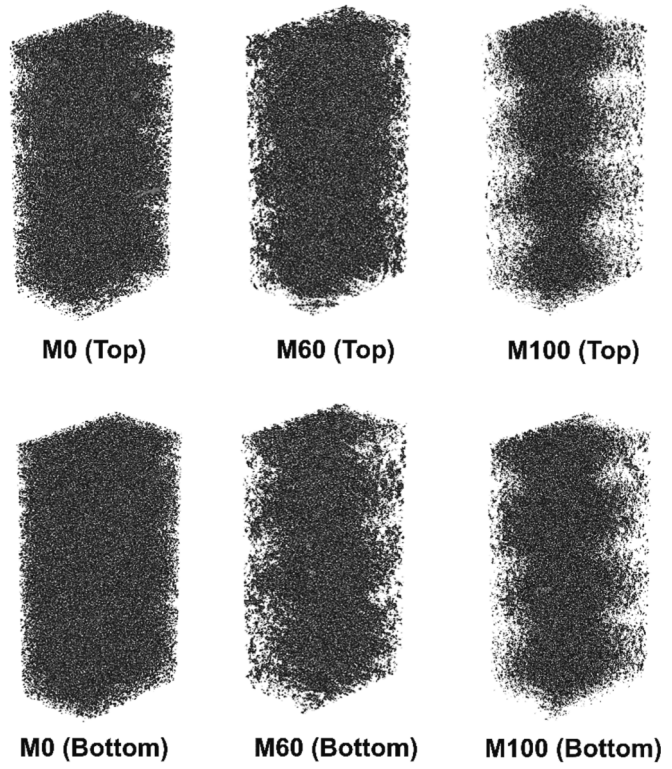

Fig. 20. Pore distributions of the target specimens at the top and bottom parts (Note: the gray represents the pores within the specimens.)

Table 6
Computed porosity from the micro-CT.

	M0	M60	M100
Top	8.96%	7.09%	2.34%
Bottom	10.20%	4.30%	3.51%

magnetite aggregates tend to affect the distribution of pores within the materials.

The pore size distribution according to the amount of magnetite aggregates was also investigated. Fig. 23 shows the pore size distribution of the measured specimens. The pore size distributions in each case and location present no clear trend, while the M0 specimen contains more proportions of relatively large pores (>0.2 mm) than the samples with magnetite. As mentioned in Table 6, the materials with magnetite aggregates assume to have denser solid structures, and this characteristic has a role in suppressing the production of relatively large pores within the materials.

In addition to the pore size, the pore shape was also characterized using the micro-CT data. Fig. 24 shows the sphericity of the pores within the materials according to the pore size. Sphericity is an index that can represent the shape of a particle, and the value becomes 1 as the shape is close to a sphere, while the value decreases as the anisotropy of a particle increases [65]. This figure indicates that the pores tend to be anisotropic as the amount of magnetite increases since more pores exist with the sphericity of 0–0.2 in the M60 and M100 specimens. From the obtained result, it can be inferred that magnetite affects the pore shape within the materials, and the dense solid structure of magnetite might contribute to this phenomenon. To investigate this more in detail, the spatial distribution of the sphericity was examined by mapping the shape parameter into the pore volume image (Fig. 25).

Fig. 25 shows the spatial distribution of the sphericity for each case. Here, the blue colour denotes the anisotropic pores with low sphericity, while the colour becomes red as the pore is close to a perfect sphere. In this figure, it can be identified that anisotropic pores with blue colour tend to increase as the amount of magnetite increases and to be distributed in the vacancy of interlayer part of the printed materials, particularly in the M60 and M100 specimens, while in the case of the M0 specimen, the pore shape in the overall sample is generally uniform and more isotropic. This confirms that the inclusion of the magnetite aggregates affects the pore size as well as pore shape, and because of their high density than the binder, the vicinity of the magnetite aggregate shows relatively high anisotropic pores, and this tendency is assumed to be clear in 3D printing materials, which significantly affected by the interlayer effect.

The comparison of solid structures can be conducted using the micro-CT data. In Fig. 26, the mean pixel values of the specimens according to the height were presented. The pixel value of micro-CT data is

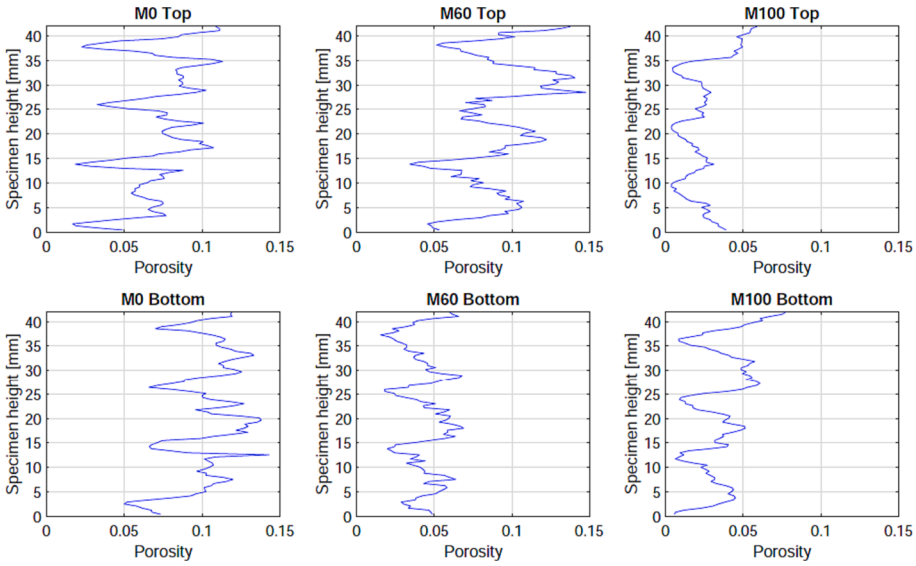

Fig. 21. Absolute porosity in relation to the specimen height.

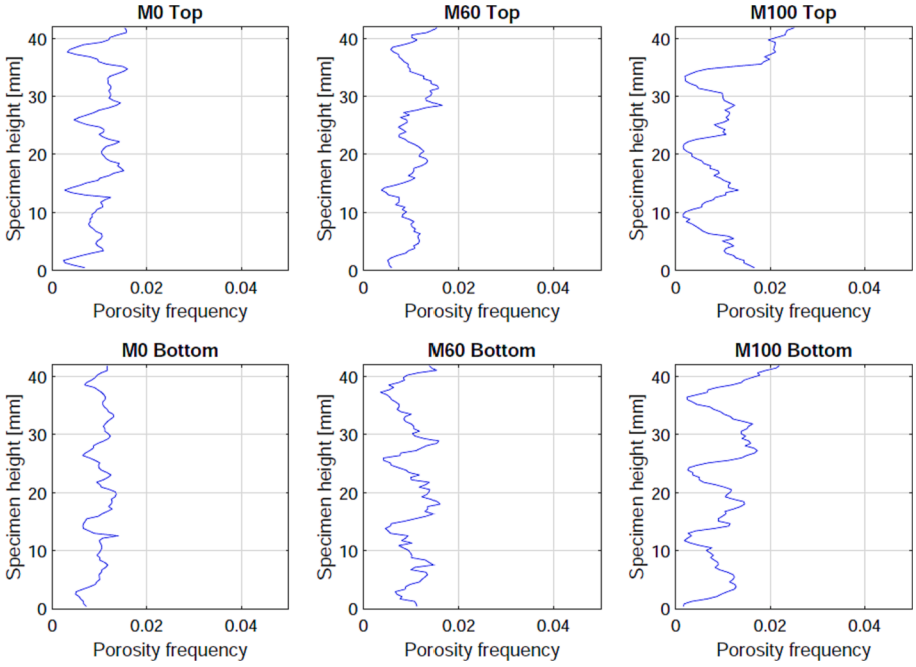

Fig. 22. Porosity frequency normalized by the total porosity of each specimen according to the specimen height.

determined by the relative density of the region, and the larger value indicates a denser solid structure. In this image, it can be clearly seen that the range of mean pixel value significantly increases as the amount of magnetite aggregates increases from M0 to M100. Based on this result, it is confirmed that the material density increases by considering the magnetite aggregate, which can affect the mechanical and thermal properties of the materials. In addition to the relative solid density, fluctuations between the layers can be seen in all cases, although the M0 can be considered almost homogeneous along the height. Therefore, it can be noted that appropriate dispersion of magnetite components needs to be carefully considered when the material is used for enhancing mechanical and radiation shielding properties.

4.5. *Radiation shielding properties*

4.5.1. *Gamma-ray attenuation performance*

Table 7 presents the results of the LAC (μ) for cast and printed specimens. There is a visible general trend that with the increase of magnetite aggregate replacement, μ also increases. No appreciable difference (Diff.% = 100 × [(print-cast)/cast]) between the cast and print specimens was found. Generally, cast specimens exhibited minimally higher values are attributed to slightly higher oven-dry density (Fig. 17). In this particular case, two factors have contributed to the slight variations between the casted and printed samples. The cast samples have a relatively higher density and porosity compared to the printed samples [54]. Higher density enhances attenuation, whereas higher porosity reduces it. With regards to gamma attenuation, the experimental results indicate that the positive and adverse factors have a nearly balanced

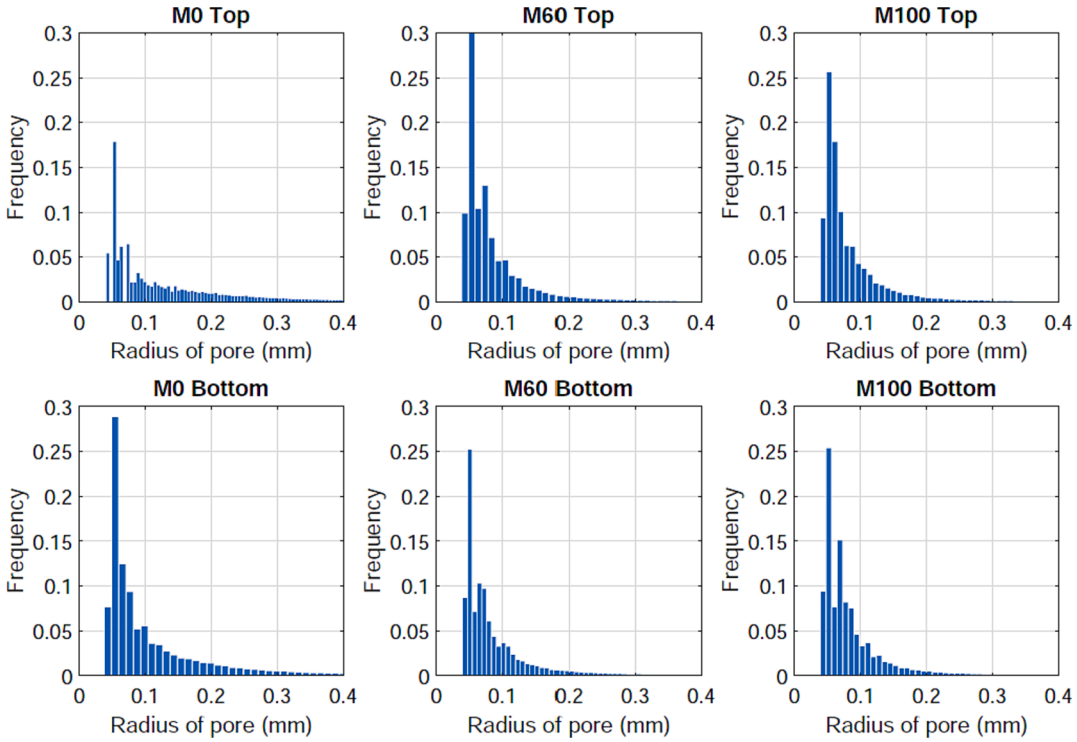

Fig. 23. Pore size distribution of the measured specimens.

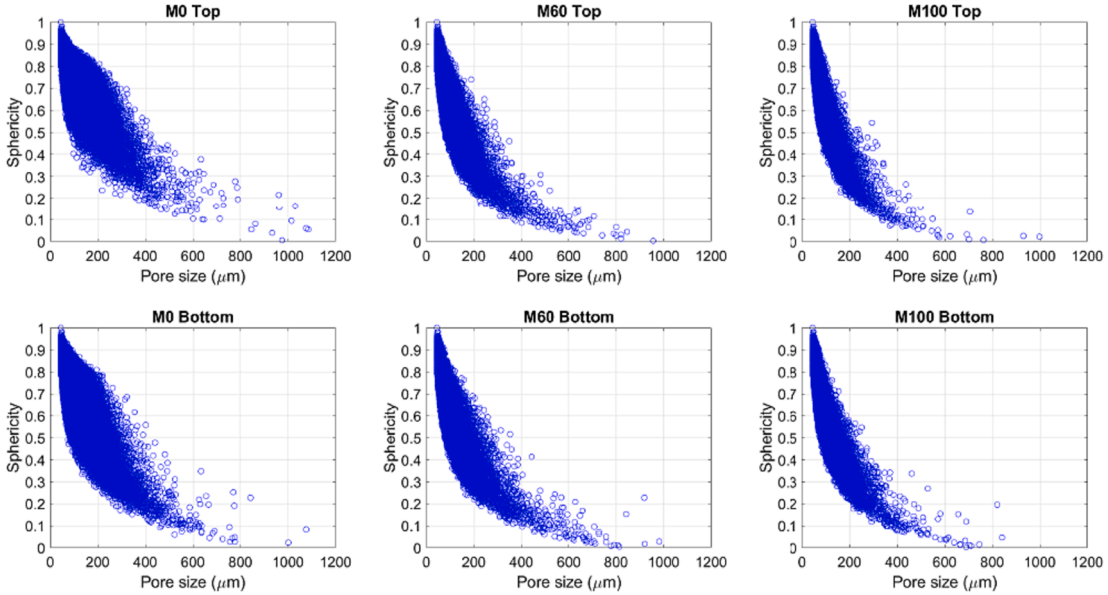

Fig. 24. Sphericity of pores within the measured specimens (Note: the sphericity of 1 indicates a whole sphere, while lower values indicate the anisotropic pores.)

overall effect, with a slight advantage for effect of density.

Due to the comparable performance of printed and cast samples against gamma-ray, to ensure proper readability, Fig. 27 presents only the results for printed specimens. Fig. 27a shows the evolution of LACs as a function of photon energy for each composition, where increasing photon energy shows decreasing μ (decreased shielding), as expected. With μ being dependent on the incident photon energy, it is also dependent on the specimen's magnetite content, where the μ of M100 exhibits maximum value.

The half-value layer thickness ($HVL = ln2/\mu$) is historically used to determine the specimen thickness required to reduce the intensity of the incident radiation by one-half. Thus, it is a more intuitive characteristics for evaluating the shielding capacity of any material, especially for engineering design purposes. The HVL data is visually illustrated in Fig. 27b. It is evident that concrete mixes with higher magnetite content exhibit lower HVL, which demonstrates the increased shielding ability of that mix. Finally, the spacing between every two curves in Fig. 27b reflects the quantitative improvement in the shielding ability. Table 8 quantifies the additional performance improvement achieved by replacing sand aggregate with 100 vol% of magnetite aggregate (M100). The improvement factor attained by the replacement of natural sand with MA reaches up to ~70%, depending on the photon energy value.

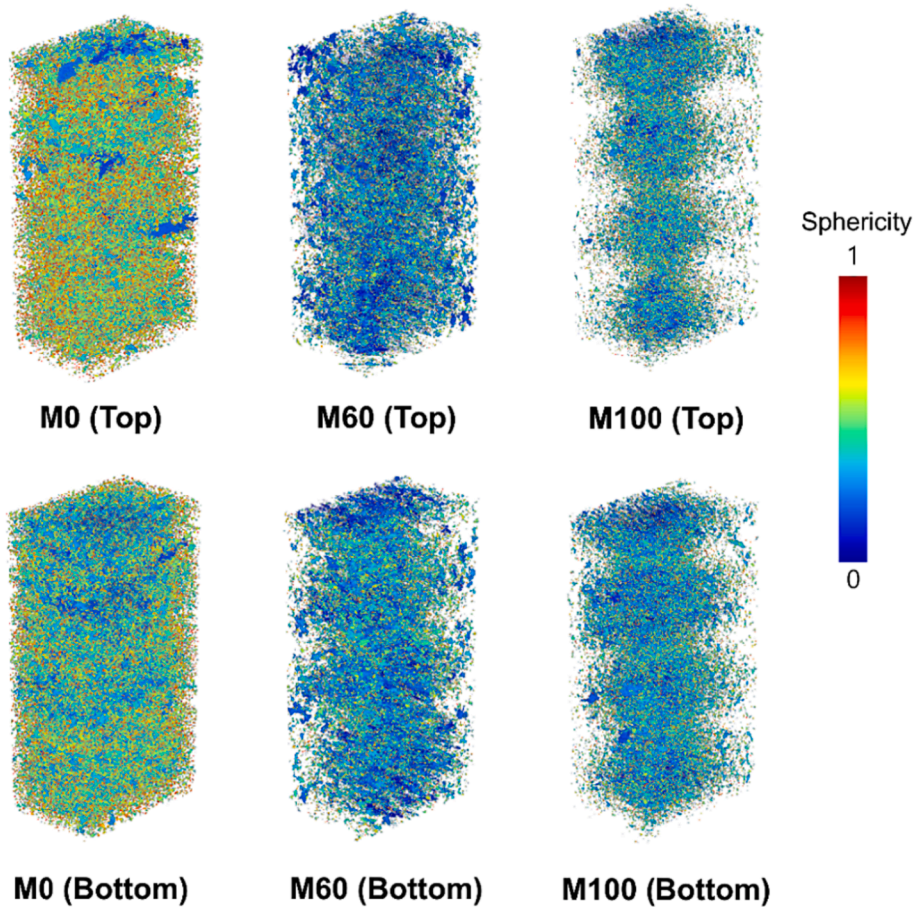

Fig. 25. Spatial distribution of the sphericity in each specimen (Note: the vacancy is the solid part, and lower sphericity (blue color) indicates more anisotropic pores.)

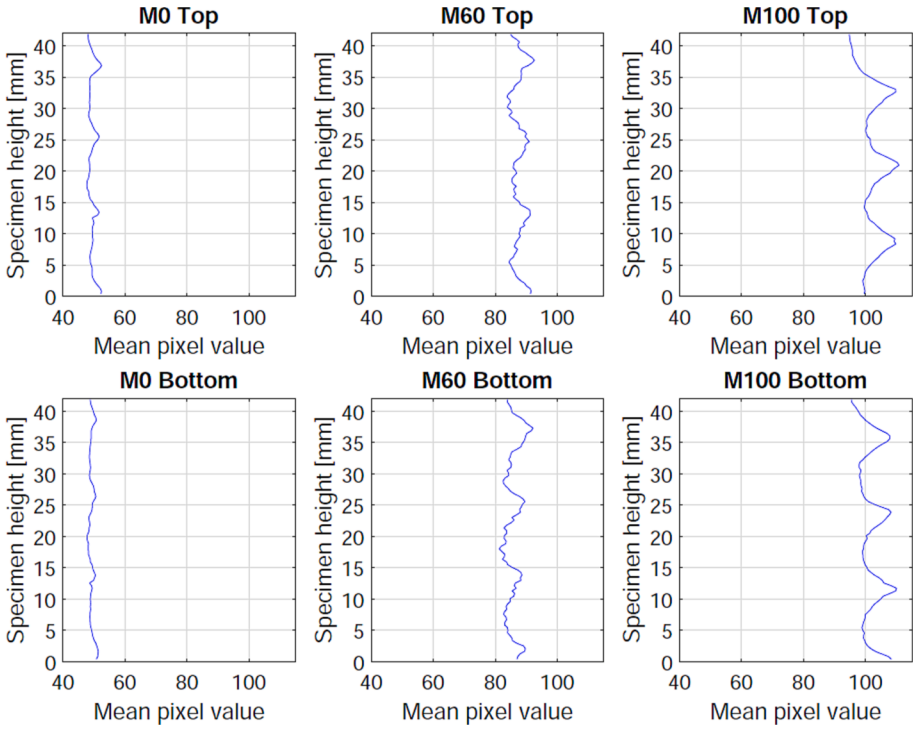

Fig. 26. Relative solid density according to the specimen height (Note: larger mean pixel value indicates higher solid density.)

Table 7
Experimental gamma-ray linear attenuation coefficients for printed and cast 3DPHWC specimens. Experimental uncertainty ≤ ±3%.

Energy (MeV)	M0 μ (cm^{-1})			M20 μ (cm^{-1})			M40 μ (cm^{-1})		
	Printed	Cast	Diff.%	Printed	Cast	Diff.%	Printed	Cast	Diff.%
0.080	0.3925	0.3917	0.20	0.4112	0.4104	0.19	0.4300	0.4292	0.18
0.238	0.3033	0.3029	0.15	0.3221	0.3216	0.14	0.3408	0.3404	0.14
0.356	0.2630	0.2633	−0.11	0.2818	0.2821	−0.10	0.3005	0.3008	−0.10
0.662	0.2112	0.2116	−0.16	0.2300	0.2303	−0.15	0.2487	0.2491	−0.14
1.173	0.2038	0.2041	−0.12	0.2226	0.2228	−0.11	0.2413	0.2416	−0.10
1.325	0.1987	0.1989	−0.09	0.2175	0.2176	−0.08	0.2362	0.2364	−0.07
2.614	0.1346	0.1347	−0.11	0.1533	0.1535	−0.10	0.1721	0.1722	−0.09

Energy (MeV)	M60 μ (cm^{-1})			M80 μ (cm^{-1})			M100 μ (cm^{-1})		
	Printed	Cast	Diff.%	Printed	Cast	Diff.%	Printed	Cast	Diff.%
0.080	0.4487	0.4479	0.18	0.4676	0.4667	0.20	0.4863	0.4854	0.17
0.238	0.3596	0.3591	0.13	0.3783	0.3779	0.12	0.3971	0.3966	0.13
0.356	0.3193	0.3196	−0.09	0.3379	0.3383	−0.13	0.3567	0.3571	−0.11
0.662	0.2675	0.2678	−0.13	0.2861	0.2866	−0.15	0.3049	0.3053	−0.14
1.173	0.2601	0.2603	−0.09	0.2790	0.2791	−0.02	0.2978	0.2978	−0.02
1.325	0.2550	0.2551	−0.07	0.2736	0.2739	−0.10	0.2924	0.2926	−0.09
2.614	0.1908	0.1910	−0.08	0.2096	0.2097	−0.04	0.2284	0.2285	−0.03

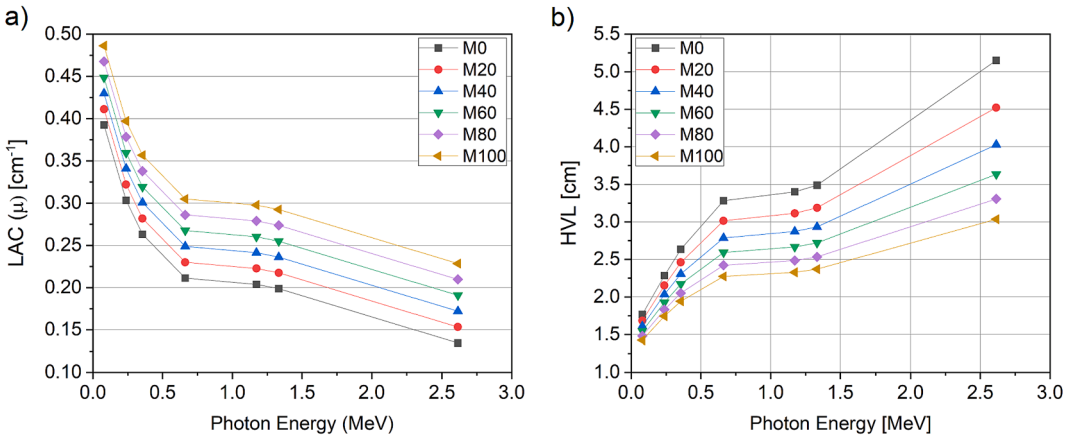

Fig. 27. Gamma-ray attenuation parameters of printed samples as function of photon energy: LACs (a) and HVLs (b).

Table 8
Improvement factor IMF% of M100 specimen related to the control sample (M0).

Energy (MeV)	0.08	0.238	0.356	0.662	1.173	1.333	2.614
Printed (IMF%)*	23.90	30.92	35.60	44.34	46.08	47.13	69.73
Cast (IMF %)	23.94	30.95	35.60	44.31	45.94	47.14	69.60

*$IMF\,\% = 100 \times (\mu_{M100} - \mu_{M0})/\mu_{M0}$.

Similar findings have been reported by several authors, including [64,66,67], who have found that incorporating hematite into concrete enhances its ability to shield against gamma rays.

4.5.2. Slow neutron attenuation performance

The results of slow neutron linear attenuations are presented in Table 9. The inclusion of magnetite aggregate to the mix causes significant increments in the neutron attenuation capacity, which is in line with other available literature studies [68]. Unlike gamma-ray shielding, results presented in Table 7, it was found that printed samples

Table 9
Experimental slow neutron linear attenuations for printed and cast 3DPHWC specimens. Experimental uncertainty ≤ ±3%.

Energy (MeV)	M0			M20			M40		
	Printed	Cast	Diff.%	Printed	Cast	Diff.%	Printed	Cast	Diff.%
Σ (cm^{-1})	0.0550	0.0524	4.93	0.0574	0.0542	6.00	0.0591	0.0548	7.96
HVL (cm)	12.61	13.23	−4.70	12.07	12.79	−5.66	11.72	12.65	−7.37

Energy (MeV)	M60			M80			M100		
	Printed	Cast	Diff.%	Printed	Cast	Diff.%	Printed	Cast	Diff.%
Σ (cm^{-1})	0.0616	0.0558	10.49	0.0634	0.0564	12.43	0.0672	0.0575	16.78
HVL (cm)	11.25	12.43	−9.50	10.94	12.30	−11.06	10.32	12.05	−14.37

exhibited a higher linear neutron attenuation coefficient (Σ_{slow}) than corresponding cast samples. In addition, with the increase of the magnetite replacement ratio, the difference between them increases, as shown in Table 9. The discrepancy between shielding ability in favor of printed specimens can be attributed to the higher porosity of the cast samples by increasing the magnetite content. Due to the low w/b and high viscosity of the mixture the vibration during the casting process results in the creation of additional voids of entrapped air, thus cast specimens might exhibit higher porosity than print specimens. This phenomenon was confirmed through mercury intrusion porosimetry (MIP) and micro-CT studies in [54]. Excess porosity will contribute to the worsening of neutron attenuation of the cast in comparison to the printed specimen. Essentially, the presence of porosity will remove the obstacles in the neutron path and consequently reduce the probability of neutron interactions with the medium. Concerning the γ-ray shielding issue, increasing the porosity in the cast sample will be compensated by contributions of iron of the magnetite aggregate, where this contribution is not significant in the slow neutron case. Finally, per Table 9, the improvement rate of the M100 sample concerning the M0 sample is 22.2% and 9.8% for printed and cast specimens, respectively.

5. Conclusions

Based on the results presented in this study following conclusions can be drawn:

- A set of 3D-printable heavyweight concretes (3DPHWC) was developed. Replacement with 40 vol% or more river sand with magnetite aggregate resulted in meeting the EN 206–1 requirement to classify the material as a heavy-weight concrete.
- As an outcome despite the inclusion of aggregate of high density no substantial differences in the fresh properties were found and all mixtures meet the printing requirements with small modifications in superplasticizer dosage. A green strength study showed that the combination of natural sand with magnetite resulted in the highest strength due to optimal packing of aggregate, while the fully magnetite mix possessed similar/lower characteristics than the control mix.
- Despite the higher self-weight of the structure, the layer's strength and stiffness were sufficient to sustain the dead load during printing. It was also confirmed that the layers remained at their height until the end of the printing process.
- The addition of magnetite aggregate led to the increase of compressive and flexural strength up to 7% for cast specimens and up to 11% for printed ones. The printing process significantly reduces the composites' strength (between 27% and 39%).
- The inclusion of magnetite aggregate into mixes resulted in an increment of the thermal conductivity of the specimens as and marginal decrement of the volumetric heat capacity of the specimens along with increasing MA dosage.
- There is a proportional relationship between the thermal conductivity, density and heat capacity of concrete. This allows for improving the predictions on the temperature development both in laboratory works and numerical modelling of mass structures, allowing for better design of elements for shielding.
- As confirmed by the micro-CT, the pore structures of 3DPHWC are strongly affected by the amount of magnetite aggregates. The porosity and general pore size tend to be smaller as more magnetite aggregates were contained, which is mainly due to the denser solid structure of magnetite.
- The pore shapes of the materials, characterized using sphericity, demonstrated that the anisotropy of the pores is noticeably affected by the magnetite aggregates, particularly in the vicinity of interlayer and magnetite. The pores within the materials with more magnetite compounds tend to be anisotropic because of the different densities of the binder and magnetite, and this is also confirmed the increase of the relative density of the materials with a larger magnetite dosage.
- Replacement of the river sand with magnetite aggregate leads to considerable improvements in the shielding performance against radiation. For printed sample M100, the improvement attained ~70% and 22% for γ-rays and slow neutrons, respectively when compared to control M0 concrete.
- In both cast and printed specimens, there are no noticeable differences between attenuation performance against gamma-rays. In contrary, the printed samples have a superiority against slow neutrons which could be attributed to differences in porosities between cast and print specimens.

CRediT authorship contribution statement

Karol Federowicz: Conceptualization, Methodology, Investigation, Validation, Visualization, Formal analysis, Data curation, Writing – original draft, Writing – review & editing. **Mateusz Techman:** Conceptualization, Methodology, Investigation, Validation, Visualization, Formal analysis, Data curation, Writing – original draft, Writing – review & editing. **Szymon Skibicki:** Conceptualization, Methodology, Investigation, Validation, Visualization, Formal analysis, Data curation, Writing – original draft, Writing – review & editing. **Mehdi Chougan:** Methodology, Validation, Writing – review & editing. **Ahmed M. El-Khayatt:** Methodology, Investigation, Validation, Visualization, Formal analysis, Data curation, Writing – original draft, Writing – review & editing. **H.A. Saudi:** Methodology, Investigation, Validation, Formal analysis, Writing – original draft. **Jarosław Błyszko:** Investigation, Validation, Writing – original draft. **Mohamed Abd Elrahman:** Methodology, Validation, Writing – original draft. **Sang-Yeop Chung:** Conceptualization, Methodology, Investigation, Validation, Visualization, Formal analysis, Data curation, Writing – original draft, Writing – review & editing. **Pawel Sikora:** Conceptualization, Methodology, Investigation, Validation, Visualization, Formal analysis, Data curation, Writing – original draft, Writing – review & editing, Project administration, Supervision.

Declaration of Competing Interest

The authors declare the following financial interests/personal relationships which may be considered as potential competing interests: Pawel Sikora reports financial support was provided by National Science Centre Poland

Data availability

Data will be made available on request.

Acknowledgements

This work was supported by the National Research Foundation of Korea (NRF) grant funded by the Korea government (Ministry of Science and ICT Grant no. NRF-2021R1A4A3030924).

Funding

This research was funded in whole by the National Science Centre, Poland within Project No. 2020/39/D/ST8/00975 (SONATA-16).

References

[1] S. Özen, C. Şengül, T. Erenoğlu, Ü. Çolak, İ.A. Reyhancan, M.A. Taşdemïr, Properties of heavyweight concrete for structural and radiation shielding purposes, Arab. J. Sci. Eng. 41 (4) (2016) 1573–1584, https://doi.org/10.1007/s13369-015-1868-6.

[2] Management of Emerging Public Health Issues and Risks, Elsevier, 2019.

[3] P. Szajerski, J. Celinska, A. Gasiorowski, R. Anyszka, R. Walendziak, M. Lewandowski, Radiation induced strength enhancement of sulfur polymer concrete composites based on waste and residue fillers, J. Clean. Prod. 271 (63) (2020), 122563, https://doi.org/10.1016/j.jclepro.2020.122563.

[4] A.M. El-Khayatt, H.A. Saudy, Preparation and characterization of zinc, lanthanum white sand glass for use in nuclear applications, Radiat. Phys. Chem. 166 (2) (2020), 108497, https://doi.org/10.1016/j.radphyschem.2019.108497.

[5] R. Peymanfar, S. Keykavous-Amand, M.M. Abadi, Y. Yassi, A novel approach toward reducing energy consumption and promoting electromagnetic interference shielding efficiency in the buildings using Brick/polyaniline nanocomposite, Constr. Build. Mater. 263 (15) (2020), 120042, https://doi.org/10.1016/j.conbuildmat.2020.120042.

[6] H.S. Alorfi, M.A. Hussein, S.A. Tijani, The use of rocks in lieu of bricks and concrete as radiation shielding barriers at low gamma and nuclear medicine energies, Constr. Build. Mater. 251 (1) (2020), 118908, https://doi.org/10.1016/j.conbuildmat.2020.118908.

[7] M.A. Masoud, A.M. El-Khayatt, W.A. Kansouh, K. Sakr, M.G. Shahien, A.M. Zayed, Insights into the effect of the mineralogical composition of serpentine aggregates on the radiation attenuation properties of their concretes, Constr. Build. Mater. 263 (2) (2020), 120141, https://doi.org/10.1016/j.conbuildmat.2020.120141.

[8] P. Sikora, M. Abd Elrahman, E. Horszczaruk, P. Brzozowski, D. Stephan, Incorporation of magnetite powder as a cement additive for improving thermal resistance and gamma-ray shielding properties of cement-based composites, Constr. Build. Mater. 204 (3) (2019) 113–121. 10.1016/j.conbuildmat.2019.01.161.

[9] M.A. Khalaf, C.C. Ban, M. Ramli, The constituents, properties and application of heavyweight concrete: A review, Constr. Build. Mater. 215 (2) (2019) 73–89, https://doi.org/10.1016/j.conbuildmat.2019.04.146.

[10] İ.B. Topçu, Properties of heavyweight concrete produced with barite, Cem. Concr. Res. 33 (6) (2003) 815–822, https://doi.org/10.1016/S0008-8846(02)01063-3.

[11] M. Techman, S. Skibicki, E. Urbańska-Galewska, Use of DMDA method for production of heavyweight concrete, MATEC Web Conf. 219 (2018) 3011, https://doi.org/10.1051/MATECCONF%2F201821903011.

[12] E. Horszczaruk, P. Brzozowski, Investigation of gamma ray shielding efficiency and physicomechanical performances of heavyweight concrete subjected to high temperature, Constr. Build. Mater. 195 (5) (2019) 574–582, https://doi.org/10.1016/j.conbuildmat.2018.09.113.

[13] A. Kukreti, P. Kundra, L. Kathait, N. Garg, S. Kumar, A review on properties of heavy weight concrete, IOP Conf. Ser.: Earth Environ. Sci. 1086 (1) (2022), 12049, https://doi.org/10.1088/1755-1315/1086/1/012049.

[14] F. Aslani, D.M. Lesslie, F. Hamidi, Development and analysis of highly workable high-strength heavyweight concrete using magnetite aggregates, Struct. Concr. 22 (S1) (2021), 242, https://doi.org/10.1002/suco.201900243.

[15] B. Badarloo, P. Lehner, R. Bakhtiari Doost, Mechanical properties and gamma radiation transmission rate of heavyweight concrete containing barite aggregates, Materials (Basel) 15 (6) (2022), https://doi.org/10.3390/ma15062173.

[16] T. Shams, M. Eftekhar, A. Shirani, Investigation of gamma radiation attenuation in heavy concrete shields containing hematite and barite aggregates in multi-layered and mixed forms, Constr. Build. Mater. 182 (9) (2018) 35–42, https://doi.org/10.1016/j.conbuildmat.2018.06.032.

[17] I.I. Bashter, A.S. Makarious, A. El-Sayed Abdo, Investigation of hematite-serpentine and ilmenite-limonite concretes for reactor radiation shielding, Ann. Nucl. Energy 23 (1) (1996) 65–71.

[18] M.A. Khalaf, C.C. Ban, M. Ramli, N.M. Ahmed, L.J. Sern, H.A. Khaleel, Physicomechanical and gamma-ray shielding properties of high-strength heavyweight concrete containing steel furnace slag aggregate, J. Build. Eng. 30 (1) (2020), 101306, https://doi.org/10.1016/j.jobe.2020.101306.

[19] Z. Wang, E. Bai, H. Huang, T. Wang, H. Sun, Study on the electromagnetic property and microwave heating efficiency of concrete with magnetite aggregate, Constr. Build. Mater. 342 (18) (2022), 128080, https://doi.org/10.1016/j.conbuildmat.2022.128080.

[20] K. Gunoglu, İ. Akkurt, Radiation shielding properties of concrete containing magnetite, Prog. Nucl. Energy 137 (1) (2021), 103776, https://doi.org/10.1016/j.pnucene.2021.103776.

[21] S.I.A. Ali, É. Lublóy, Fire resistance properties of heavyweight magnetite concrete in comparison with normal basalt- and quartz-based concrete, J. Therm. Anal. Calorim. 84 (2) (2022) 23, https://doi.org/10.1007/s10973-022-11407-3.

[22] M.P. Tinoco, É.M. de Mendonça, L.I.C. Fernandez, L.R. Caldas, O.A.M. Reales, R. d. Toledo Filho, Life cycle assessment (LCA) and environmental sustainability of cementitious materials for 3D concrete printing: A systematic literature review, J. Build. Eng. 52 (2022), 104456, https://doi.org/10.1016/j.jobe.2022.104456.

[23] M. Chougan, S.H. Ghaffar, P. Sikora, S.-Y. Chung, T. Rucinska, D. Stephan, A. Albar, M.R. Swash, Investigation of additive incorporation on rheological, microstructural and mechanical properties of 3D printable alkali-activated materials, Mater. Des. 202 (2021), 109574, https://doi.org/10.1016/j.matdes.2021.109574.

[24] E. Ivaniuk, M. Friedrich Eichenauer, Z. Tošić, S. Müller, D. Lordick, V. Mechtcherine, 3D printing and assembling of frame modules using printable strain-hardening cement-based composites (SHCC), Mater. Des. 219 (3) (2022), 110757, https://doi.org/10.1016/j.matdes.2022.110757.

[25] B. Raphael, S. Senthilnathan, A. Patel, S. Bhat, A review of concrete 3D printed structural members, Front. Built Environ. 8 (2023), 690, https://doi.org/10.3389/fbuil.2022.1034020.

[26] J. Xiao, G. Ji, Y. Zhang, G. Ma, V. Mechtcherine, J. Pan, L. Wang, T. Ding, Z. Duan, S. Du, Large-scale 3D printing concrete technology: Current status and future opportunities, Cem. Concr. Compos. 122 (2021), 104115, https://doi.org/10.1016/j.cemconcomp.2021.104115.

[27] Y.W.D. Tay, Y. Qian, M.J. Tan, Printability region for 3D concrete printing using slump and slump flow test, Compos. B Eng. 174 (2019), 106968, https://doi.org/10.1016/j.compositesb.2019.106968.

[28] D. Falliano, D. de Domenico, G. Ricciardi, E. Gugliandolo, 3D-printable lightweight foamed concrete and comparison with classical foamed concrete in terms of fresh state properties and mechanical strength, Constr. Build. Mater. 254 (11) (2020), 119271, https://doi.org/10.1016/j.conbuildmat.2020.119271.

[29] S. Skibicki, M. Techman, K. Federowicz, N. Olczyk, M. Hoffmann, Experimental study of hardened Young's modulus for 3D printed mortar, Materials (Basel) 14 (24) (2021), https://doi.org/10.3390/ma14247643.

[30] M. Hoffmann, S. Skibicki, P. Pankratow, A. Zieliński, M. Pajor, M. Techman, Automation in the construction of a 3D-printed concrete wall with the use of a lintel gripper, Materials (Basel) 13 (8) (2020), https://doi.org/10.3390/MA13081800.

[31] EN 12390-15: Testing hardened concrete, Adiabatic method for the determination of heat released by concrete during its hardening process, (2019).

[32] EN 12390-14: Testing hardened concrete: Semi-adiabatic method for the determination of heat released by concrete during its hardening process, (2018).

[33] M.A. Glinicki, Jaskulski, R., Pichór, W., Dąbrowski, M., Sobczak, M. (Eds.), Investigation of Thermal Properties of Shielding Concrete, Poland, (2015).

[34] EN 1015-3: Methods of test for mortar for masonry, Determination of consistence of fresh mortar (by flow table).

[35] PN-B-04500: Building mortars, Physical properties and strength tests, (1985).

[36] M.A. Abd Elaty, M.F. Ghazy, Flow properties of fresh concrete by using modified geotechnical Vane shear test, HBRC J. 8 (3) (2019) 159–169, https://doi.org/10.1016/j.hbrcj.2012.07.001.

[37] S. Skibicki, M. Pułtorak, M. Kaszyńska, M. Hoffmann, E. Ekiert, D. Sibera, The effect of using recycled PET aggregates on mechanical and durability properties of 3D printed mortar, Constr. Build. Mater. 335 (2) (2022), 127443, https://doi.org/10.1016/j.conbuildmat.2022.127443.

[38] M. Kaszyńska, S. Skibicki, M. Hoffmann, 3D concrete printing for sustainable construction, Energies 13 (23) (2020), 6351, https://doi.org/10.3390/en13236351.

[39] B. Mazhoud, A. Perrot, V. Picandet, D. Rangeard, E. Courteille, Underwater 3D printing of cement-based mortar, Constr. Build. Mater. 214 (2019) 458–467, https://doi.org/10.1016/j.conbuildmat.2019.04.134.

[40] A. Perrot, D. Rangeard, A. Pierre, Structural built-up of cement-based materials used for 3D-printing extrusion techniques, Mater. Struct. 49 (4) (2016) 1213–1220, https://doi.org/10.1617/s11527-015-0571-0.

[41] EN 1015-11: Methods of test for mortar for masonry, Determination of flexural and compressive strength of hardened mortar, (2019).

[42] ISO 22007-2: Plastics - Determination of thermal conductivity and thermal diffusivity, ransient plane heat source (hot disc) method, (2015).

[43] M. Abd Elrahman, S.-Y. Chung, P. Sikora, T. Rucinska, D. Stephan, Influence of nanosilica on mechanical properties, sorptivity, and microstructure of lightweight concrete, Materials (Basel) 12 (19) (2019), https://doi.org/10.3390/ma12193078.

[44] S.-Y. Chung, J.-S. Kim, D. Stephan, T.-S. Han, Overview of the use of micro-computed tomography (micro-CT) to investigate the relation between the material characteristics and properties of cement-based materials, Constr. Build. Mater. 229 (550) (2019), 116843, https://doi.org/10.1016/j.conbuildmat.2019.116843.

[45] Ł. Skarżyński, J. Tejchman, Experimental investigations of damage evolution in concrete during bending by continuous micro-CT scanning, Mater. Charact. 154 (4) (2019) 40–52, https://doi.org/10.1016/j.matchar.2019.05.034.

[46] L. Kong, M. Ostadhassan, X. Hou, M. Mann, C. Li, Microstructure characteristics and fractal analysis of 3D-printed sandstone using micro-CT and SEM-EDS, J. Pet. Sci. Eng. 175 (7) (2019) 1039–1048, https://doi.org/10.1016/j.petrol.2019.01.050.

[47] P. Sikora, S.-Y. Chung, M. Liard, D. Lootens, T. Dorn, P.H. Kamm, D. Stephan, M. Abd Elrahman, The effects of nanosilica on the fresh and hardened properties of 3D printable mortars, Constr. Build. Mater. 281 (23) (2021), 122574, https://doi.org/10.1016/j.conbuildmat.2021.122574.

[48] MATLAB. R2021a, The MathWorks Inc, (2021).

[49] P. Sikora, A.M. El-Khayatt, H.A. Saudi, S.-Y. Chung, D. Stephan, M. Abd Elrahman, Evaluation of the effects of bismuth oxide (Bi2O3) micro and nanoparticles on the mechanical, microstructural and γ-ray/neutron shielding properties of Portland cement pastes, Constr. Build. Mater. 284 (1) (2021), 122758, https://doi.org/10.1016/j.conbuildmat.2021.122758.

[50] A.U. Rehman, J.-H. Kim, 3D concrete printing: A systematic review of rheology, mix designs, mechanical, microstructural, and durability characteristics, Materials (Basel) 14 (14) (2021), https://doi.org/10.3390/ma14143800.

[51] R.J.M. Wolfs, F.P. Bos, T.A.M. Salet, Early age mechanical behaviour of 3D printed concrete: Numerical modelling and experimental testing, Cem. Concr. Res. 106 (3) (2018) 103–116, https://doi.org/10.1016/j.cemconres.2018.02.001.

[52] G. Sotorrío Ortega, J. Alonso Madrid, N.O.E. Olsson, J.A. Tenorio Ríos, The application of 3D-printing techniques in the manufacturing of cement-based construction products and experiences based on the assessment of such products, Buildings 10 (9) (2020) 144, https://doi.org/10.3390/buildings10090144.

[53] T.T. Le, S.A. Austin, S. Lim, R.A. Buswell, A.G.F. Gibb, T. Thorpe, Mix design and fresh properties for high-performance printing concrete, Mater. Struct. 45 (8) (2012) 1221–1232, https://doi.org/10.1617/s11527-012-9828-z.

[54] P. Sikora, M. Techman, K. Federowicz, A.M. El-Khayatt, H.A. Saudi, M. Abd Elrahman, M. Hoffmann, D. Stephan, S.-Y. Chung, Insight into the microstructural and durability characteristics of 3D printed concrete: Cast versus printed specimens, Case Studies, Constr. Mater. 17 (2022) e01320.

[55] T. Ding, J. Xiao, F. Qin, Z. Duan, Mechanical behavior of 3D printed mortar with recycled sand at early ages, Constr. Build. Mater. 248 (2005) (2020), 118654, https://doi.org/10.1016/j.conbuildmat.2020.118654.
[56] S. Skibicki, P. Jakubowska, M. Kaszyńska, D. Sibera, K. Cendrowski, M. Hoffmann, Early-age mechanical properties of 3D-printed mortar with spent garnet, Materials (Basel) 15 (1) (2021), https://doi.org/10.3390/ma15010100.
[57] A. Perrot, A. Pierre, S. Vitaloni, V. Picandet, Prediction of lateral form pressure exerted by concrete at low casting rates, Mater. Struct. 48 (7) (2015) 2315–2322, https://doi.org/10.1617/s11527-014-0313-8.
[58] S.H. Bong, M. Xia, B. Nematollahi, C. Shi, Ambient temperature cured 'just-add-water' geopolymer for 3D concrete printing applications, Cem. Concr. Compos. 121 (6) (2021), 104060, https://doi.org/10.1016/j.cemconcomp.2021.104060.
[59] EN 206: Concrete, Specification, performance, production and conformity, (2013).
[60] S. Ismail Ahmed Ali, E. Lublóy, Effect of elevated temperature on the magnetite and quartz concrete at different W/C ratios as nuclear shielding concretes, Nucl. Mater. Energy 33 (2) (2022), 101234, https://doi.org/10.1016/j.nme.2022.101234.
[61] R. Jaskulski, M.A. Glinicki, W. Kubissa, M. Dąbrowski, Application of a non-stationary method in determination of the thermal properties of radiation shielding concrete with heavy and hydrous aggregate, Int. J. Heat Mass Transf. 130 (2019) 882–892, https://doi.org/10.1016/j.ijheatmasstransfer.2018.07.050.
[62] S. Yu, M. Xia, J. Sanjayan, L. Yang, J. Xiao, H. Du, Microstructural characterization of 3D printed concrete, J. Build. Eng. 44 (2021), 102948, https://doi.org/10.1016/j.jobe.2021.102948.
[63] K. Federowicz, M. Kaszyńska, A. Zieliński, M. Hoffmann, Effect of curing methods on shrinkage development in 3D-printed concrete, Materials (Basel) 13 (11) (2020), https://doi.org/10.3390/ma13112590.
[64] O. Gencel, A. Bozkurt, E. Kam, T. Korkut, Determination and calculation of gamma and neutron shielding characteristics of concretes containing different hematite proportions, Ann. Nucl. Energy 38 (12) (2011) 2719–2723, https://doi.org/10.1016/j.anucene.2011.08.010.
[65] Y. Shin, H.M. Park, J. Park, H. Cho, S.-E. Oh, S.-Y. Chung, B. Yang, Effect of polymer binder on the mechanical and microstructural properties of pervious pavement materials, Constr. Build. Mater. 325 (7) (2022), 126209, https://doi.org/10.1016/j.conbuildmat.2021.126209.
[66] A. Un, F. Demir, Determination of mass attenuation coefficients, effective atomic numbers and effective electron numbers for heavy-weight and normal-weight concretes, Appl. Radiat. Isot. 80 (2013) 73–77, https://doi.org/10.1016/j.apradiso.2013.06.015.
[67] M.A. Saafan, Z.A. Etman, A.S. Jaballah, M.A. Abdelati, Strength and nuclear shielding performance of heavyweight concrete experimental and theoretical analysis using WinXCom program, Prog. Nucl. Energy 160 (4) (2023), 104688, https://doi.org/10.1016/j.pnucene.2023.104688.
[68] B. Oto, A. Gür, E. Kavaz, T. Çakır, N. Yaltay, Determination of gamma and fast neutron shielding parameters of magnetite concretes, Prog. Nucl. Energy 92 (1) (2016) 71–80, https://doi.org/10.1016/j.pnucene.2016.06.011.